Materials Today Bio 22 (2023) 100727

Contents lists available at ScienceDirect

Materials Today Bio

journal homepage: www.journals.elsevier.com/materials-today-bio

A cost-effective and enhanced mesenchymal stem cell expansion platform with internal plasma-activated biofunctional interfaces

Anyu Zhang [a,b,e,1], Johnny Kuan Un Wong [c,d,e,1], Katazhyna Redzikultsava [a,b], Mark Baldry [a,b,e], Seyedeh KH. Alavi [a,b], Ziyu Wang [c,d], Eveline van Koten [b], Anthony Weiss [c,d], Marcela Bilek [a,b,c,e], Giselle C. Yeo [c,d,2,**], Behnam Akhavan [a,b,e,f,g,2,*]

[a] School of Biomedical Engineering, University of Sydney, NSW 2006, Australia
[b] School of Physics, University of Sydney, NSW 2006, Australia
[c] Charles Perkins Centre, University of Sydney, NSW 2006, Australia
[d] School of Life and Environmental Sciences, University of Sydney, NSW 2006, Australia
[e] Sydney Nano Institute, University of Sydney, NSW 2006, Australia
[f] School of Engineering, University of Newcastle, Callaghan, NSW 2308, Australia
[g] Hunter Medical Research Institute (HMRI), Precision Medicine Program, New Lambton Heights, NSW, 2305, Australia

ARTICLE INFO

Keywords:
Biomimetic
Tissue engineering
Scaffolds
Porous polymer structure
Mesenchymal stem cell
Cell expansion system

ABSTRACT

Mesenchymal stem cells (MSCs) used for clinical applications require *in vitro* expansion to achieve therapeutically relevant numbers. However, conventional planar cell expansion approaches using tissue culture vessels are inefficient, costly, and can trigger MSC phenotypic and functional decline. Here we present a one-step dry plasma process to modify the internal surfaces of three-dimensional (3D) printed, high surface area to volume ratio (high-SA:V) porous scaffolds as platforms for stem cell expansion. To address the long-lasting challenge of uniform plasma treatment within the micrometre-sized pores of scaffolds, we developed a packed bed plasma immersion ion implantation (PBPI^3) technology by which plasma is ignited inside porous materials for homogeneous surface activation. COMSOL Multiphysics simulations support our experimental data and provide insights into the role of electrical field and pressure distribution in plasma ignition. Spatial surface characterisation inside scaffolds demonstrates the homogeneity of PBPI^3 activation. The PBPI^3 treatment induces radical-containing chemical structures that enable the covalent attachment of biomolecules via a simple, non-toxic, single-step incubation process. We showed that PBPI^3-treated scaffolds biofunctionalised with fibroblast growth factor 2 (FGF2) significantly promoted the expansion of MSCs, preserved cell phenotypic expression, and multipotency, while reducing the usage of costly growth factor supplements. This breakthrough PBPI^3 technology can be applied to a wide range of 3D polymeric porous scaffolds, paving the way towards developing new biomimetic interfaces for tissue engineering and regenerative medicine.

1. Introduction

Mesenchymal stem cells (MSCs) are multipotent adult stem cells isolated from various adult tissues, such as bone marrow, adipose tissue, and umbilical cord [1,2]. MSCs demonstrate outstanding potential in the treatment of diseases such as graft-versus-host disease (GvHD) [3,4], osteoarthritis [5,6], cardiovascular disease [7,8] and also as an emerging component in regenerative medicine applications for tissues such as bone and cartilage [9–11]. These therapeutic benefits arise from the capabilities of MSCs for self-renewal, differentiation, homing, intercellular communication, and immunomodulation [9,12].

The limited amount of MSCs harvested from patients cannot fulfil the high cell doses required for clinical applications, prompting the need for *ex vivo* cell expansion. MSCs, as adherent cells, require surfaces to attach

* Corresponding author. School of Biomedical Engineering, University of Sydney, NSW 2006, Australia.
** Corresponding author. Charles Perkins Centre, University of Sydney, NSW 2006, Australia.
E-mail addresses: giselle.yeo@sydney.edu.au (G.C. Yeo), Behnam.Akhavan@newcastle.edu.au, behnam.akhavan@sydney.edu.au (B. Akhavan).
[1] Contributed equally to this work.
[2] Co-senior authors.

https://doi.org/10.1016/j.mtbio.2023.100727
Received 17 March 2023; Received in revised form 30 June 2023; Accepted 7 July 2023
Available online 7 July 2023

to and proliferate. However, conventional planar (2D) expansion platforms are inefficient due to a small cell growth area relative to the high volume of culture media required. Furthermore, prolonged periods of culture on standard tissue culture plastics may lead to phenotypic and functional decline, which subsequently lowers the therapeutic potential of the harvested MSCs [13,14].

To overcome these hindrances in the expansion of MSCs, advances have been made to improve cell yield and cell quality using three-dimension (3D) substrates with high-surface-area-to-volume ratios (high-SA:V), such as microcarriers in bioreactors [13,15] or hollow fibres in perfusion systems [16,17]. The high-SA:V substrates provide a sufficiently large surface area for MSC adhesion and proliferation. They can also be surface modified to enhance biocompatibility; for example, by increasing hydrophilicity to improve cell adhesion [18,19] and tailoring surface topography to regulate cell behaviour [20,21]. In addition, the large surface available in 3D porous materials can be engineered with biological signals to create a biomimetic environment that directs cell properties, including cell growth [22].

Surface biofunctionalisation can be achieved through either a simple physical adsorption process or covalent wet-chemistry methods. Physical adsorption of biomolecules on scaffolds is simple and easy to scale up, but it has major drawbacks. Physiosorbed proteins tend to denature due to strong hydrophobic interactions [23] and may detach from the surface due to desorption or exchange processes such as the Vroman effect [24], triggering unexpected adverse responses [25,26]. Wet-chemistry methods address these problems, but the industrial scalability of these methods is limited due to the time-consuming and complicated sequence of chemical steps involved [23]. This complexity is also typically associated with problems in, for example, regulatory approval, chemical waste generation and management. Furthermore, wet chemistry methods are often substrate-dependent, necessitating specific surface chemistry for different substrates and targeted biomolecules, which heightens the challenges of industrial scalability [23].

Dry plasma-based approaches for covalent surface immobilisation of biomolecules hold great promise as emerging alternatives to wet-chemistry methods without the above limitations. In these dry and environmentally friendly processes, plasma is utilised to create chemical functional groups on the surface or long-lived radicals embedded inside the surface to covalently attach biomolecules onto solid materials [23,27].

We have pioneered a plasma immersion ion implantation (PI^3) technology to create a high concentration of surface-embedded radicals in polymeric materials for direct covalent attachment of a wide range of biomolecules and hydrogels [27–32]. Unlike conventional glow discharge plasma treatment processes that result in shallow surface modification of polymers, PI^3 treatment creates radical reservoirs tens to hundreds of nanometres deep below the polymer surface through ion bombardment under negative high voltage (HV). The long-lived radicals, stabilised within π conjugated carbon clusters, migrate to the surface over many months through thermally activated processes, where they facilitate covalent attachment of molecules [33,34] in a conformation- and density-tuneable manner [35].

Despite these intriguing advantages, applying the PI^3 process to porous scaffolds is not trivial. The orthodox view in the field is that plasma technologies are not suitable for modifying the internal surfaces of 3D micrometre-sized porous structures [36–39], due to insufficient diffusion of active plasma species into the internal pore network [38,40]. Previous studies showed plasma diffusion into only a depth of 300 μm into a PCL/$CHCl_3$ scaffold with 150–300 μm pore sizes [41]. While flipping scaffolds during plasma treatment can improve treatment depth [42], this rudimentary approach is only applicable to scaffolds of limited height. Plasma penetration can also be increased by placing the scaffolds at the outlet of a plasma reactor, relying on a vacuum to pull active plasma species into the porous scaffolds [43]. This method, however, generates heterogeneously modified materials with a limited range of geometry and pore size [40]. Recently, a dielectric barrier discharge (DBD) reactor was studied to modify the internal surfaces of polyetheretherketone (PEEK) scaffolds [44]. However, the treatment was achieved in pores that are larger than 1 mm, which can also be treated using other plasma methods relying on diffusion [40,45]. Our group has recently demonstrated plasma modification of the inner surfaces of hollow fibre capillary bundles enclosed in a cassette, using a packed bed plasma immersion ion implantation ($PBPI^3$) approach [46].

Building on this $PBPI^3$ approach, here we present a new strategy to directly ignite plasmas inside the micrometre-sized (200 μm) pores of 3D-printed polystyrene scaffolds for surface biofunctionalisation (see Fig. 1). Challenging the current thinking in the plasma surface engineering field, we provide evidence that this strategy enables a surface activation of the entire porous network of scaffolds for subsequent covalent linkage of biomolecules. Aided by integrated experiments and modelling, our findings provide new knowledge elucidating the interplay between gas pressure and electric field distribution to achieve optimal treatment throughout the scaffold structures. We demonstrate the use of this technology for the development of a bespoke 3D MSC culture platform that stably captures mitogenic growth factors to promote cell expansion while preserving functional phenotype. This industrially scalable plasma-based process paves the way for the development of new classes of biomimetic porous materials for applications across a range of areas, including regenerative medicine and tissue engineering.

2. Materials and methods

2.1. Fused filament fabrication

Porous structure designs with an orthogonal layer configuration (filament spacing: 600 μm; filament diameter: 200 μm) were built using Solidworks, computer-aided design (CAD) software. Scaffolds were additively manufactured from high impact polystyrene (HiPS) filaments (RS Pro 1.75 mm Natural HiPS 3D Printer Filament, RS Components Pty Ltd) via an extrusion 3D printer (Dreamer 3D printer, FlashForge Corporation, China). The scaffolds were generated using the orthogonal layer structure in both columns (30 mm length, 10 mm diameter) and mesh (1 mm thickness, 10 mm diameter) forms, as shown in Fig. 2a. The extruder temperature was set at 245 ± 2 °C, and the bed temperature at 110 ± 2 °C. The room temperature was kept at 25 ± 2 °C.

2.2. Packed-bed plasma immersion ion implantation ($PBPI^3$) treatment of scaffolds

$PBPI^3$ treatment of additively manufactured porous scaffolds was performed using a custom-made, tubular $PBPI^3$ system composed of two separate vacuum lines connected to an inner sample holder and an outer glass chamber. The design of this system is schematically shown in Fig. 2b and c. The 3D-printed scaffolds were loaded into the middle of the glass sample holder, as shown in Fig. 2b. The outer glass chamber (length: 1000 mm, diameter: 170 mm) and the glass sample holder were pumped down using a turbo molecular pump and a screw pump, respectively. The pressure at both ends of the glass sample holder was measured using two pressure gauges. After the base pressure inside the glass sample holder (1.2×10^{-1} Torr) and in the outer glass chamber (5×10^{-3} Torr) was achieved, nitrogen (N_2) gas (0.5 standard cubic centimetre per minute (sccm)) was injected through an Alicat mass flow controller into the gas sample holder. The inlet and outlet pressures were then adjusted by closing the tube valve until they reached the desired stable experimental pressure. The power system consisted of a negative HV electrode connected to a pulsed voltage source (RUP 6–25, GBS Electronics, Germany) and two earthed electrodes. Both earthed

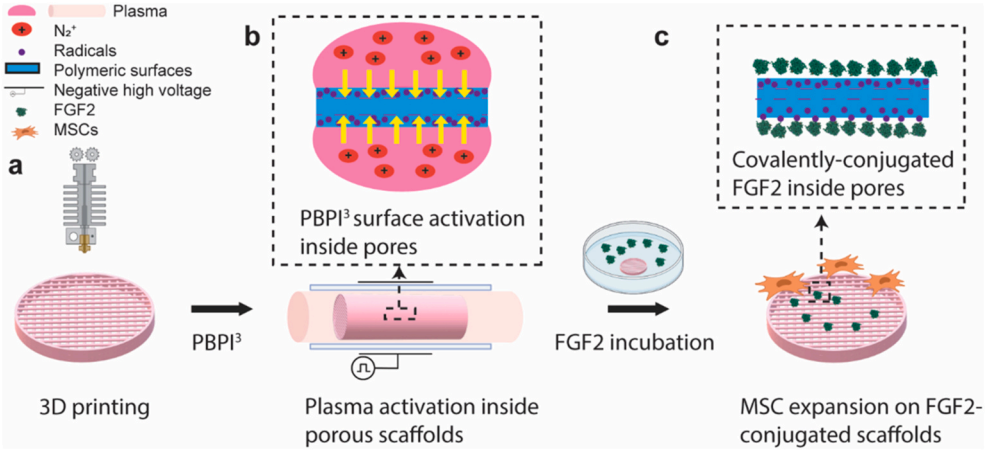

Fig. 1. Schematic illustration of PBPI^3-based surface functionalisation inside porous scaffolds for MSC expansion: a) 3D printing of polymer scaffold; b) Plasma activation inside porous scaffolds for PBPI^3 surface activation; c) Reagent-free covalent immobilisation of FGF2 onto PBPI^3-activated scaffolds for MSC expansion.

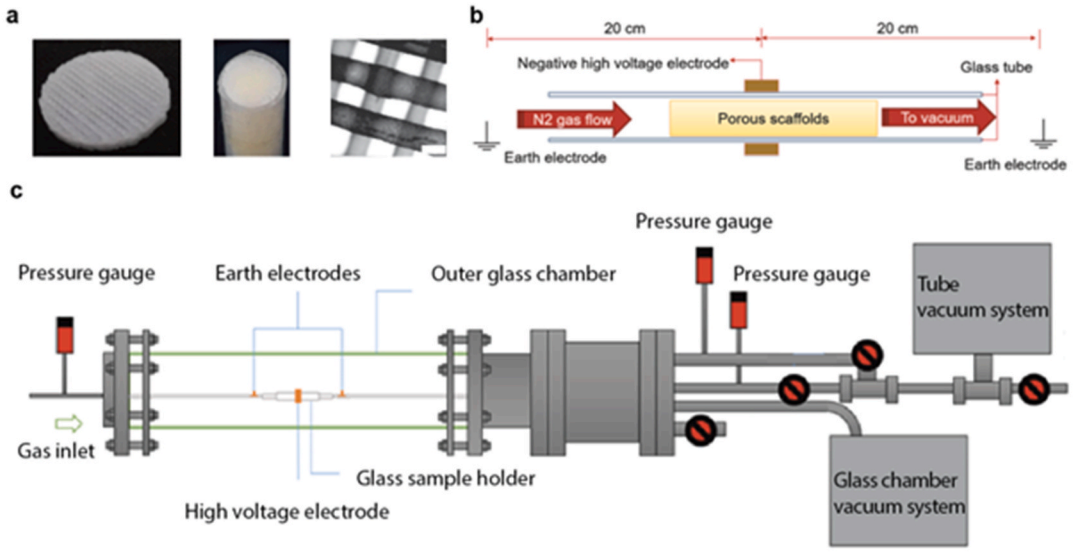

Fig. 2. **a)** The 3D printed scaffold in forms of a mesh and a column with a pore size of 200 ± 25 μm (Scale bar: 200 μm). **b)** Schematic illustration of the scaffold and electrode positions in the custom-made PBPI^3 system. **c)** Schematic illustration of the customised PBPI^3 system used for the activation of 3D printed scaffolds.

electrodes were placed 20 cm away from the centre of the negative HV electrode, and were in contact with the gas. The nitrogen plasma was discharged between the HV electrode and the two earthed electrodes. PBPI^3 was achieved by optimising HV pulses and working pressure, in the ranges of 4–8 kV and 1–3 Torr, respectively.

2.3. Numerical modelling

The flow of nitrogen gas through the scaffolds and the electrostatic field established within the reactor were simulated in 3D using the finite element software COMSOL Multiphysics, and is detailed in Redzikultsava et al. [47]. The nitrogen was modelled as a laminar, fully compressible flow in a steady state under a range of conditions. The electrostatic field arising from different electrode configurations and applied potentials was simulated independently of the flow. The models represented pre-breakdown conditions and were used to understand how different reactor setups might influence scaffold treatment. The modelled scenarios reflected the experimental setup and included various scaffold geometries at working pressures of 1, 2, 3 Torr with a HV electrode (length:10 mm) modelled with applied potentials of 4, 6, and 8 kV. The kinetic energy ($KE_e = \mathbf{E}q_e\lambda$) of the electrons was calculated throughout the computational domain and used as an indicator for the favourability of plasma breakdown, where **E** is the electric field, q_e is the electron charge, $\lambda = (\sqrt{2\pi d^2 n})^{-1}$ is the particle mean free path, d is the kinetic diameter, and n is the number density.

2.4. Micro attenuated total reflectance Fourier transform infrared spectroscopy (micro ATR FTIR)

A Hyperion 2000-ATR micro ATR FITR spectrometer (Bruker Optics, USA) was used for the spatially resolved analysis of the surface chemistry of untreated (UT) and PBPI^3-treated scaffolds. All micro ATR FTIR measurements were carried out using samples aged one week after the PBPI^3 treatment. The micro ATR FTIR instrument was equipped with an optical microscope and an ATR crystal covering an area with a diameter of 100 μm. The scaffold samples were opened along their long axis, providing easy access for analysis of the internal scaffold network. To evaluate treatment uniformity, five positions (Fig. 3e) were selected for measurements in septuplicate with 30 scans taken at a resolution of 4 cm^{-1}. The spectra were normalised on the C–H bond vibration absorbance peak at 1493 cm^{-1}. The height of O–H peaks, a broad absorbance

peak between 3300 and 3500 cm^{-1}, for untreated and $PBPI^3$ treated samples were imported into GraphPad Prism 9 for statistical analysis.

2.5. X-ray photoelectron spectroscopy (XPS)

A K-Alpha+ system (Thermo Scientific American) was used to obtain XPS spectra for analysing the surface chemistry of the untreated and the $PBPI^3$-treated scaffolds. The measurement spot size was 200 μm. Survey spectra were collected through 10 scans in the range of −10 to 1350 eV with a pass energy of 200 eV and resolution of 1.0 eV. High-resolution spectra of carbon (C1s) and nitrogen (N1s) were recorded through 10 scans at pass energy of 50 eV and a resolution of 0.1 eV. Thermo Scientific Avantage data system was used for spectral calibrations, atomic concentration calculations and peak fittings.

2.6. Time-of-flight secondary ion mass spectrometry (ToF-SIMS)

A nano TOF equipment (PHITRIFT V, Chanhassen, MN) was used to obtain ToF-SIMS spectra at an operation voltage of 30 eV with a pulsed liquid (79 Auþ) metal primary ion source (LMIG). SIMS was set as a positive mode at a base pressure below 5×10^{-6} Pa for all measurements. An electron flood gun and Ar^+ ions (10 eV) were used to achieve dual charge neutralisation for all measurements. Five evenly distributed spots with measurement areas of 350 × 350 μm were taken on each sample to collect ToF-SIMS spectra. All spectra were analysed using WincadenceN software (version 1.8.1, Physical Electronics).

2.7. Optical emission spectroscopy (OES)

An Acton Spectra Pro 2750 spectrometer (Princeton Instruments, Acton, M, USA) was used for OES measurements. The plasma emission was collected by a fused-silica optical fibre bundle, 1 mm in diameter, connected to the entrance slit of the spectrometer. A 1200 lines mm^{-1} grating was used, providing a nominal resolution of 0.0140 nm at 300 nm, and 0.0120 nm at 750 nm. The plasma emission spectra were captured using an ICCD with a 1024 × 1024 pixel array (Princeton Instrument, PI-MAX) placed at the spectrometer's exit.

2.8. Electron paramagnetic resonance (EPR)

A SpinscanX EPR spectrometer (Adani, Belarus) was used to perform EPR spectroscopy, measuring the concentration of unpaired electrons in both UT and $PBPI^3$-treated scaffolds. UT and $PBPI^3$-treated scaffolds were halved, and four cut pieces from each were adhered to a double-sided tape and attached to the bottom of an EPR glass tube. The samples were consistently positioned at a fixed location in the EPR cavity. Spectra were obtained under the following conditions: a central magnetic field of 336 mT, microwave frequency of 9.38 GHz, microwave power of 0.9 mW, modulation amplitude of 200 mT, and the field modulation frequency was set at 100 kHz. The spectrometer was calibrated using Mn-doped MgO. An average of ten scans was taken per sample. The same $PBPI^3$-treated scaffolds were reused to measure radical density as a function of storage time at room temperature. The resulting EPR spectra were then processed using the Origin 2022 software.

2.9. Scanning electron microscope (SEM)

A Phenom XL Scanning Electron Microscope (PhenomWorld, Eindhoven, The Netherlands) was used in secondary electron detector (SED) mode to obtain images of untreated and $PBPI^3$-treated scaffolds. The scaffolds were first coated with Au/Pd inside a sputter coater (SC7620 Quorum) with a coating thickness of 16 nm. Images were obtained at a voltage of 10 kV, a pressure of 1 Pa, and a working distance of 5 mm in SEM mode.

2.10. Wettability analysis

Wettability evaluation of untreated and $PBPI^3$-treated scaffolds was carried out by placing the samples into MilliQ water within 1 h (hr) and one week after the $PBPI^3$ treatment. The wettability of samples was also assessed by evaluating the penetration of a water droplet (1 μL) placed on the surfaces of scaffolds within 1 h after $PBPI^3$ treatment. These tests were carried out using a Theta Lite (Biolin Scientific) optical goniometer controlled by One Attension software (version 3.1, 2017).

2.11. Protein coating

Untreated or PI^3-treated PS films or $PBPI^3$-treated HiPS scaffolds were submerged in various concentrations (10–8000 ng/mL) of fibroblast growth factor 2 (FGF2) (Thermo Fisher Scientific) dissolved in PBS (10 mM sodium phosphate, 150 mM NaCl) (Thermo Fisher Scientific). Chemically similar PS films were used in lieu of scaffolds to optimise protein coating conditions. Sterilised hollow glass tubes were used to keep films or scaffolds submerged in the protein solution. Samples were incubated at 4 °C for 16 h or at room temperature (RT) for 3 h, then washed with PBS to remove excess unbound protein.

2.12. Micro bicinchoninic acid assay (μBCA)

Untreated and $PBPI^3$-treated HiPS scaffolds were coated with bovine serum albumin (BSA) by immersing in BSA solution (65 mg/mL) overnight at room temperature. Half of the BSA-coated samples were then incubated in 5% (w/v) sodium dodecyl sulphate (SDS) at 37 °C for 20 h. For comparison, the rest of the BSA-coated samples were immersed in Milli-Q water under the same conditions. After detergent washing, SDS-washed samples were rinsed three times in Milli-Q water. Samples were incubated in the Pierce μBCA working reagent (Thermo Scientific) at 37 °C for 2 h. The scaffolds were removed, and absorbances were read at 562 nm with a plate reader (TECAN Infinite M1000 Pro).

2.13. Enzyme-linked immunosorbent assay (ELISA)

Untreated and $PBPI^3$-treated HiPS scaffolds were coated with FGF2 as described. Where indicated, half of the samples were immersed in 2% (v/v) Tween-20, heated to 60 °C for 20 min, and then washed with PBS three times. Unwashed scaffolds were kept in PBS. All samples were blocked with 3% (w/v) bovine serum albumin (BSA) (Merck) for 1 h at RT, then rinsed once with PBS. Surface-bound FGF2 was detected with 1 μg/mL mouse monoclonal anti-FGF2 antibody (Abcam) for 1 h at RT and washed three times with PBS. A 1:5000 dilution of goat anti-mouse horseradish peroxidase-conjugated secondary antibody (Abcam) was added to the samples and incubated at 4 °C overnight. Samples were washed three times with PBS, further rinsed in a large volume of PBS and transferred to a fresh 48-well plate. ABTS substrate (1.1 mg/mL of 2,2′-azino-bis(3-ethylbenzothiazoline-6-sulfonic acid) diammonium salt, 0.05% (v/v) H_2O_2, 10 mM CH_3COONa, 5 mM Na_2HPO_2) was added to each sample for 20 min at RT, and absorbances were read at 405 nm with a plate reader (TECAN Infinite M1000 Pro).

2.14. Confocal imaging

To visualise the covalent attachment and homogenous distribution of biomolecules on $PBPI^3$-treated scaffolds, Cyanine5 (Cy5)-conjugated goat anti-rabbit IgG protein (Invitrogen) was used as a model biomolecule. Untreated and $PBPI^3$-treated scaffolds were incubated in 4 μg/mL IgG/PBS solution for 2 h at room temperature. Protein-coated samples were immersed in 2% (v/v) Tween-20 and heated to 60 °C for 1 h to remove physisorbed IgG molecules. The samples were then washed with PBS three times. The scaffolds were imaged using a confocal microscope (Nikon C2). The laser was set at 640 nm with a laser power of 2.0. Image processing was performed using Fiji software.

2.15. Human bone marrow-derived MSC culture

Human bone marrow-derived MSCs from a 35-year-old Hispanic female were purchased from American Type Culture Collection (VA, USA). The MSCs were cultured in Alpha Minimum Essential Medium (αMEM) (Merck) supplemented with 10% (v/v) MSC-verified foetal bovine serum (Thermo Fisher Scientific), 1% (v/v) L-glutamine (Merck) and 50 U/mL penicillin/streptomycin (Thermo Fisher Scientific). Cells were incubated at 37 °C in 5% CO2. MSCs between passages 5–8 were used for all cell experiments.

2.16. Scaffold sterilisation

All films and scaffolds for cell culture use were disinfected under ultraviolet (UV) light in a Class II biosafety cabinet for 30 min on each side and washed three times with PBS prior to protein coating. The glass tubes used to hold down films and scaffolds in wells were disinfected in 80% (v/v) ethanol for a minimum of 24 h, washed three times with PBS, and soaked in PBS overnight prior to use.

2.17. Cell quantification on 2D films

MSCs were seeded on untreated and PI^3-treated polystyrene (PS) films at 5000 cells/cm^2 concentration. The PI^3 treatment of 2D PS films was previously described [48]. After 3 and 7 days in culture, cell numbers were assayed by DNA quantification using a CyQUANT cell proliferation kit (Thermo Fisher Scientific). Culture media was removed before the MSC-laden films were transferred to a new plate and frozen at −80 °C for a minimum of 24 h. Cells were lysed by freeze-thawing and in 1:20 CyQUANT lysis buffer. CyQUANT dye was added to the cells at a 1:400 ratio and was incubated in the dark for 15 min. After incubation, aliquots were transferred to a new plate. Sample fluorescence was measured at 480 nm excitation and 520 nm emission using a TECAN Infinite M1000 Pro plate reader.

2.18. Cell proliferation assay

Sterilised untreated and PI^3-treated PS films or $PBPI^3$-treated scaffolds with and without FGF2 were seeded with 5000 cells per scaffold. Culture media was changed every 2 days. At 3-, 7-, 10-, and 14-days post-seeding, samples were washed with PBS, fixed for 20 min with 4% (w/v) formaldehyde, rinsed with PBS thrice, and stored in PBS at 4 °C until all timepoints were collected. At the last timepoint, PBS was removed, and cells were stained for 1 h in 0.1% (w/v) crystal violet in 0.2 M 2-(N morpholino) ethanesulfonic acid (MES) buffer, pH 5. Stained films and scaffolds were rinsed with distilled water thrice and blotted dry before being transferred to a new 48-well plate for bright-field imaging. Samples were imaged using a Zeiss AXIO vertA1 microscope. After imaging, cell staining was solubilised in 10% (v/v) acetic acid for 15 min. Aliquots were taken after 30 s shaking, and read at 570 nm using a plate reader (TECAN Infinite M1000 Pro).

2.19. Cell metabolic activity assay

The metabolic activity of cells cultured in untreated and $PBPI^3$-treated scaffolds with and without FGF2 was assessed using Alamar Blue, a resazurin sodium salt (Sigma). At specific timepoints post-seeding, a working concentration of Alamar Blue (0.005% (w/v) in PBS) was added to the culture medium and incubated for 2.5 h in a 37 °C incubator with 5% CO_2. Following the incubation period, 100 μL of the culture medium from each sample was transferred to a 96-well plate. Fluorescence was measured using a plate reader (Tecan M1000 Pro), with excitation set at 560 nm and emission at 590 nm. Culture medium containing Alamar Blue from cell-free tissue culture plastic or scaffolds was used for background subtraction. Cell numbers were determined using a standard curve generated from serially diluted cells. After fluorescence measurements, wells containing samples were washed once with PBS, incubated in fresh culture medium, and returned to the incubator until the next timepoint.

2.20. Whole scaffold imaging

Cells were seeded on untreated and $PBPI^3$-treated HiPS scaffolds with or without FGF2, as described for the cell proliferation assay. At 1, 4, 7-, 10-, 12-, and 14-days post-seeding, scaffolds were washed with PBS and fixed with 10% (v/v) formalin (Merck) for 20 min at RT, followed by three PBS washes. Quenching was carried out with 0.2 M glycine for 20 min at RT, followed by three PBS washes. Cells were permeabilised using 0.1% (v/v) Triton X-100 (Thermo Fisher Scientific) for 5 min at RT, washed thrice with PBS and incubated with NucBlue Live ReadyProbe (Thermo Fisher Scientific) and ActinRed 555 ReadyProbe (Thermo Fisher Scientific) for 15 min at RT. Finally, the scaffolds were washed 3 times with PBS. The scaffolds were imaged using a Nikon NiE widefield fluorescence microscope with built-in stitching function. Images were processed using Max Intensity followed by the Red Hot Lookup Table (LUT) with ImageJ software.

2.21. Flow cytometry

MSCs were grown on tissue culture plastic, or on $PBPI^3$-treated HiPS scaffolds with or without FGF2 (20 ng/mL) for 9 and 14 days. Cells were harvested via enzymatic dissociation using 0.05% (w/v) trypsin-EDTA and resuspended at 1×10^5 cells/mL in PBS with 5% (v/v) foetal bovine serum. Expression of surface markers was characterised with CD73-FITC, CD90-APC, CD105-PerCP/Cy5.5, and a cocktail of lineage negative antibodies ($CD45^-$, $CD34^-$, CD11b-, $CD19^-$, HLA-DR-PE) (BD Biosciences) using a BD LSR II flow cytometer.

2.22. Gene expression analysis

MSCs were grown on 2D TCP and 3D $PBPI^3$-treated PS scaffolds with and without FGF2 (20 ng/mL) coating for 14 days. Cells were washed thrice with PBS and lysed. Sample RNA was isolated using the Aurum Total RNA Mini kit (Bio-Rad), and synthesised into cDNA using the iScript cDNA synthesis kit (Bio-Rad). The cells were characterised for their expression of Oct4 markers via real-time quantitative polymerase chain reaction (qPCR) using a LightCycler 480 instrument (Roche). Transcript levels were normalised against GAPDH expression, and expressed as fold changes relative to the gene expression levels of cells grown on 2D TCP without FGF2. Primer sequences and the qPCR parameters are provided in Supplementary Tables S1 and S2, respectively.

2.23. Statistical analyses

Results were expressed as mean ± standard error ($n \geq 3$). A one-way or two-way analysis of variance (ANOVA) was performed with Tukey's multiple comparison test to determine statistical significance. Statistical significance in figures was presented as * or Φ, $p < 0.05$; ** or ΦΦ, $p < 0.01$; *** or ΦΦΦ, $p < 0.001$; and **** or ΦΦΦΦ, $p < 0.0001$.

3. Results and discussion

3.1. $PBPI^3$ activation of porous scaffolds

In conventional plasma surface treatment systems, active plasma species do not sufficiently penetrate into porous structures with pore sizes smaller than 1 mm [40]. Here we employed a new strategy, referred as packed-bed plasma immersion ion implantation ($PBPI^3$), to overcome this limitation by directly igniting plasma inside the porous structures. In this arrangement, a porous HiPS scaffold was inserted into a glass tube wrapped by a copper electrode to form a dielectric barrier discharge (DBD) system. The electrode under negative HV was placed in

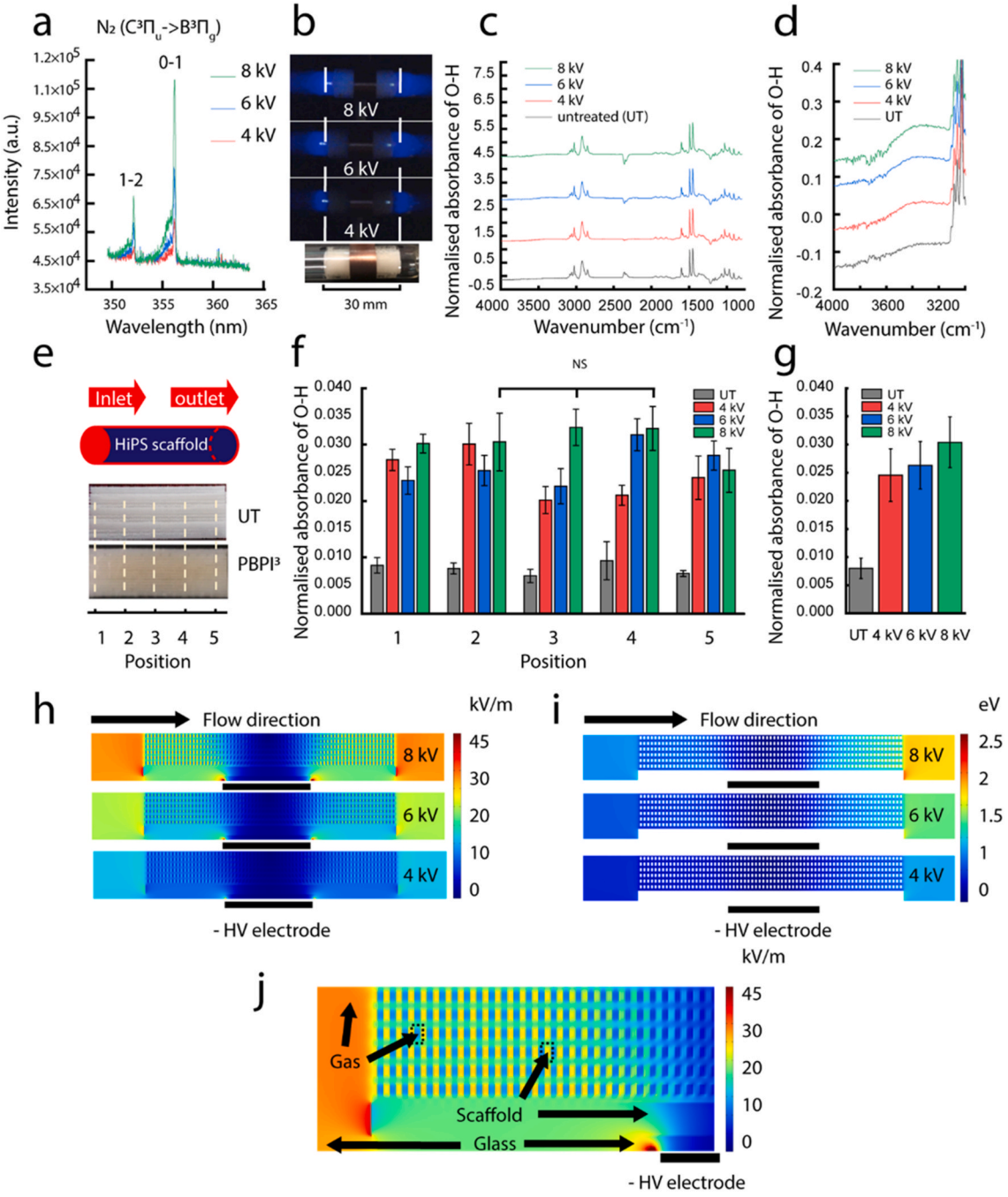

Fig. 3. HiPS scaffolds treated with PBPI^3 as a function of voltage. **a)** Emission spectrum of the discharge in the tube inlet at 3 cm from the inlet of the scaffold. It shows two peaks of the second positive system of nitrogen $N_2(C^3\Pi_u->B^3\Pi_g)$ with corresponding vibrational quantum numbers ν'-ν'' [1-2,0-1]. The intensity significantly increases with applied HV. **b)** Optical images of plasma breakdown at a voltage of 4, 6, or 8 kV. **c)** Representative ATR FTIR spectra (800-4000 cm^{-1}), and **d)** high-resolution FTIR spectra (3000-4000 cm^{-1}) for PBPI^3-treated scaffolds with applied HV of 4, 6, and 8 kV. **e)** Schematic illustration and optical images for the spatial micro ATR FTIR measurements. **f)** Mapped absorbance of O–H bonds in the PBPI^3-treated surface of the scaffolds against the untreated (UT) scaffolds at 4, 6, and 8 kV (n = 9 for PBPI^3-treated samples, n = 3 for untreated samples, normalised to the absorbance of the C–H bond vibration at 1493 cm^{-1}). No significant difference was observed from position 2 to 4. **g)** The absorbance of O–H bonds in the PBPI^3-treated scaffolds at 4,6 and 8 kV (n = 45) against the untreated scaffolds (n = 15), pooled from all measurements along the longitudinal cross-section of the scaffolds. Numerical modelling of **h)** electric field distribution inside scaffolds at 4, 6, 8 kV**; i)** distribution of electron kinetic energy over a mean free path inside scaffolds at 4, 6, 8 kV; **j)** magnified electric field distribution inside pores at 8 kV.

the middle of the glass tube so that the insulating scaffold was positioned in the discharge path (Fig. 2b). The new arrangement was expected to yield plasma ignition inside the scaffolds, followed by ion implantation and radical creation within the internal surfaces of the scaffolds. To evaluate this hypothesis, we initially optimised the homogeneity of PBPI^3 treatment inside scaffolds by independently varying the HV and working pressure.

We began with plasma ignition at 4, 6, and 8 kV with pressure kept constant at 1 Torr to examine the chemistry of the plasma discharge using OES. The voltage optimisation range was determined by the minimum breakdown voltage and the maximum achievable voltage without arcing. Fig. 3a shows the representative OES spectra of the nitrogen discharge in the range of 351–365 nm recorded at 3 cm to the inlet of the scaffold for the three applied voltages. Two peaks were

observed at the wavelengths of 353.7 nm and 357.7 nm. These peaks are assigned to transitions 1–2 and 0–1 of the second positive system of nitrogen ($C^3\Pi_u \rightarrow B^3\Pi_g$), respectively. The optical emission intensity (OEI) of both the peaks increased with the applied voltages, which was consistent with the trend of increasing plasma intensity as a function of voltage as visually observed in optical images (Fig. 3b). This increase is because the corresponding increased electric field transfers more energy to electrons in the plasma with increasing applied voltage. The electrons, in turn, collide with gas molecules increasing the number of species in excited states in the plasma, resulting in higher spectral intensity.

We applied micro ATR FTIR to analyse the surface chemistry inside the PBPI^3-treated scaffolds. Fig. 3c and **d** show ATR-FTIR spectra of the samples from 4 to 8 kV in the range of 800–4000 cm^{-1} and 3000-4000 cm^{-1}, respectively. For all voltages, a new broad peak was observed in the region of 3100–3700 cm^{-1}, which was assigned to the hydroxyl (O–H) stretching vibration band [49]. The O–H band was only found on the PBPI^3-treated surfaces while no oxygen was present in the discharge gas (99.999% nitrogen) or in the chemistry of untreated HiPS. The new O–H bond can be explained by the post-reaction between the PBPI^3--treated surface and the atmosphere [49]. During PBPI^3 treatment, the applied negative voltage, which is capacitively coupled to the polymeric scaffold, accelerates nitrogen ions from the plasma towards the polymeric substrate. These energetic ions then penetrated into the substrate surface and break bonds along their collision cascades, creating highly reactive radicals inside the substrate surfaces. Using 2D polymeric surfaces, we have previously shown that such surface-embedded radicals migrate to the substrate-air interface [34] and react with atmospheric oxygen-containing species, forming OH groups [49]. In Fig. 3d, the magnified spectra in the range of 3000–4000 cm^{-1} more clearly demonstrate that the broad O–H band has an increasing trend as a function of the HV magnitude. The FTIR results agree well with the observed increasing trend of OEI, as shown in Fig. 3a. The formation of new OH groups on the surfaces is an indicator of the surface treatment degree. We used the normalised absorbance intensity of the O–H bond vibration (normalised to the 1451 cm^{-1} C–H vibration absorbance peak) to assess the surface treatment uniformity inside the scaffolds.

To evaluate the PBPI^3 treatment inside the scaffolds, micro ATR FTIR measurements in the O–H region were mapped at 5 locations along the longitudinal cross-section of the scaffold with equal spacing (7.5 mm), as schematically indicated in Fig. 3e. Fig. 3f shows a significant increase ($p < 0.0001$) of the O–H absorbance on PBPI^3-treated scaffolds against the untreated controls at all the locations regardless of the applied voltages. The increase indicated that the entire structure of the scaffolds was successfully treated using PBPI^3. Of particular importance was the middle position [3] of the scaffolds, where a significant increase of O–H was observed, providing evidence that even the centre of the scaffold was successfully treated by the nitrogen plasma.

We further interpreted the distribution of the mapped O–H absorbance values to assess the PBPI^3 treatment homogeneity. The scaffolds treated at 8 kV displayed similar levels of O–H absorbance across the scaffold (position 2–4) with no significant difference, demonstrating the highest uniformity in comparison with the surface treatment at 4 and 6 kV (Fig. 3f). In particular, the middle position [3] had a similar extent of surface chemistry change compared to nearby positions (2 & 4). The two ends of the scaffolds, upstream (position 1) and downstream (position 5), were not counted for uniformity assessment because they were subjected to mechanical deformation and possible contamination during production, and thus removed after PBPI^3 treatment. The uniform treatment inside the internal structure achieved using our PBPI^3 strategy is of high significance because no strategy has yet demonstrated homogenous surface treatment inside scaffolds with pore sizes smaller than 200 μm.

This uniformity in surface treatment was also visually observed in the optical images (Fig. 3e). The PBPI^3-treated samples showed a uniformly distributed darkening on the cross-section compared to the untreated samples. This darkening results from PBPI^3-induced carbonisation on carbon-rich polymers, i.e. the loss of hydrogen [33] and formation of sp2-bonded π-conjugated graphitic clusters [33,49]. The correlation between PBPI^3 treatment homogeneity and the applied HV can be further explained by the optical images obtained from the plasma discharge (Fig. 3b). From these images, plasma formation inside the scaffolds was visually observed only at 8 kV. This observation correlates well with the homogeneity of FTIR surface chemistry measurements (Fig. 3e and f). It is, therefore, plausible to suggest that the plasma discharge achieved inside the scaffold underpins the homogeneous surface modification. Fig. 3g shows the O–H absorbance values pooled together from all the measurement spots along the longitudinal cross-section of the scaffolds. The increasing trend of O–H absorbance value as a function of applied voltage indicated that the highest degree of surface modification was achieved at 8 kV. Taken together, we conclude that homogeneous plasma modification inside the entire porous network of the scaffolds can be achieved via our PBPI^3 approach at an applied potential at the high voltage electrode of 8 kV.

The treatment process was simulated under a range of conditions to understand the underlying mechanism behind the uniform surface treatment throughout the scaffold structures. The electrical field distribution inside the scaffold was modelled as a function of the applied potential (Fig. 3h). The electrical field inside the scaffold pores, which is linearly related to the acceleration of electrons in the field, increased in magnitude with increasing potential. The kinetic energy gained by an electron depends on the magnitude of this acceleration as well as on the distance to its next collision which can be estimated by the mean free patch (λ). The likelihood of forming an ionisation cascade, which creates a plasma, increases with the rise of kinetic energy of the electrons prior to each collision. Hence the kinetic energy up to collision acquired by electrons at any given location can be considered to be an indicator of the favourability of conditions for plasma breakdown there. This kinetic energy increases as a function of applied potential as plotted in Fig. 3i. This increase in electrical field and kinetic energy agrees well with the trends observed in OES and surface treatment as a function of applied potential (Fig. 3a, g). It shows that the plasma breakdown inside the scaffolds is more favourable at higher voltages.

The enhanced electrical field within the scaffold pores is more clearly observed in Fig. 3j. The numerical model revealed that the electric field was notably stronger inside the scaffold pores than in the struts. Meanwhile, as a function of applied potential, the electrical field was only enhanced in the pores, while it remained almost unchanged in the struts. The enhanced electric field in the pores can be explained by the polarisation induced on the dielectric scaffold material [50,51]. An externally applied electric field on an insulating material causes a dipole moment in the material, enhancing the electric field outside the dielectric material. This enhanced electric field enables plasma creation inside the 3D pore network. Our observation agrees with a previous numerical study in which it was shown that the electrical field was enhanced in between the dielectric material due to polarisation [51].

In addition to the applied potential, the working pressure of nitrogen gas at which the PBPI^3 treatment is carried out is also a key parameter that can regulate the plasma activation inside the scaffold. Mean free path (MFP), defined by the working pressure, is the average distance a particle can travel before colliding with other particles. Ionising collisions between the electrons and the nitrogen molecules create a plasma, while the nitrogen ions that collide with the scaffold surfaces yield PBPI^3 surface treatment. To evaluate the role of working pressure on surface treatment, we varied the gad pressure from 1 to 3 Torr with a volumetric gas flow of 0.5 sccm. The optimal applied potential of 8 kV at the high

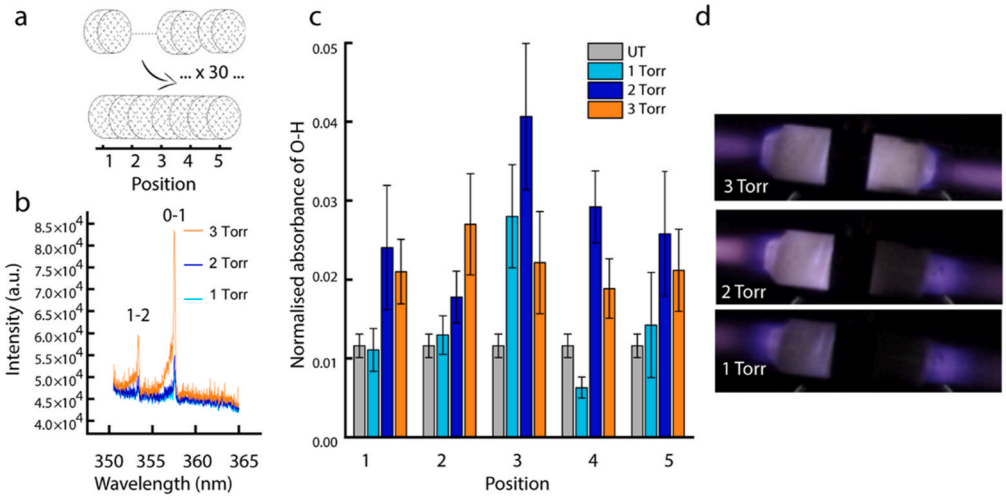

Fig. 4. HiPS scaffolds treated with PBPI^3 as a function of working pressures. **a)** Schematic diagram of the assembly of 30 scaffold disks, each with a thickness of 1 mm. **b)** Emission spectra of the N_2 discharge at 8 kV for 1, 2, and 3 Torr that were observed in the tube inlet at 3 cm from the inlet of the scaffold. The spectra show two emission peaks of the second positive system of nitrogen $N_2(C^3\Pi_u\text{->}B^3\Pi_g)$ with corresponding vibrational quantum numbers ν'-ν'' [1-2,0-1]. The optical emission intensity increases as a function of pressure. **c)** The mapped ATR-FTIR absorbance of O–H bonds in the untreated and PBPI^3-treated scaffolds at 1, 2, and 3 Torr ($n > 6$, normalised to the absorbance of the C–H bond vibration at 1493 cm^{-1} of HiPS). **d)** Optical images of plasma breakdown at 1, 2 and 3 Torr.

voltage electrode was kept consistent for all the subsequent experiments. In this experiment set up, 30 scaffold disks with a thickness of 1 mm were plasma-treated together in an assembly (Fig. 4a) to produce PBPI^3-activated scaffold disks for MSC studies.

Fig. 4b shows the optical emission spectra of nitrogen plasma, showing peaks related to transitions 1–2 and 0–1 of the N2 (C3Πu→B3Πg) band collected at various working pressures. The OEIs of both the peaks recorded at the wavelength of 353.7 nm and 357.7 nm for 3 Torr were higher than those measured for the 1 and 2 Torr conditions. The higher working pressure results in an increased number of nitrogen molecules and an associated increase in their collisions with electrons, thus leading to a higher number of excited molecules and radiative photons.

To evaluate the influence of working pressure on the uniformity of surface treatment, we mapped the ATR-FTIR O–H absorbance values as shown in Fig. 4c. The scaffolds treated at 3 Torr showed the least difference in the levels of O–H absorbance across its cross-section (position 1–5). Although a similar level of homogeneity was observed for scaffolds treated at 1 Torr, O–H absorbance values were not significantly different from that of the untreated control. From these results, it can be concluded that the scaffolds treated at 3 Torr demonstrate the highest homogeneity of surface treatment, a conclusion that is in agreement with the optical image obtained from the plasma discharged at this working pressure (Fig. 4d). To gain insights into the plasma breakdown and resulting surface treatment inside the scaffolds, we modelled the MFP distribution for the working pressures tested experimentally, with the results and discussions presented in supplementary figures (Fig. S1). Briefly, by increasing the working pressure from 1 to 3 Torr, the MFP reduced from 24.5 μm to 16.2 μm with an improved homogeneity.

3.2. Surface characterisation of the optimised PBPI^3-activated scaffolds

XPS and ToF-SIMS were used to further assess the surface chemistry of scaffolds PBPI^3 treated using the optimal processing parameters of HV = 8 kV and P = 3 Torr. Fig. 5a shows the XPS survey spectra obtained for the untreated and PBPI^3-treated scaffolds taken from the middle of the assembly (position 3). For the untreated HiPS control, the XPS survey spectrum showed only signals from carbon atoms. This chemistry is consistent with the chemical structure of HiPS, which consists of the conjugated diene hydrocarbon chain and phenyl groups as shown in Fig. 5b [52]. Following the PBPI^3-treatment, the nitrogen atomic concentration increases from 0% to 14.45%. This change in surface chemistry agrees well with the mechanism of PBPI^3 treatment, in which nitrogen ions in the plasma are implanted into the surface after acceleration by the negative HV [48]. This increase in atomic nitrogen concentration was also accompanied by an increase in oxygen atomic concentration from 0% to 14.8%, correlating well with the FTIR results (Fig. 3), where OH group vibrations appeared as a result of post-treatment oxidation reactions between the surface radicals and atmospheric oxygen [49].

To further elucidate the changes in surface chemistry as a result of PBPI^3 treatment, four peaks, i.e., C–C (sp2)/C–H at binding energy (BE) ≅ 284.6 eV, C–O/C–N at BE ≅ 286.4 eV, C=O/N–C=O at BE ≅ 287.4 eV, and COOH at BE ≅ 289.0 eV [53], were fitted in the C1s high-resolution spectra, shown in Fig. 5c, with the calculated area percentages indicated in caption. The C1s peak from the untreated sample was symmetric, composed of only C–C and C–H with an area percentage of 100, consistent with the chemical structure of the HiPS. Upon PBPI^3 treatment, the C1s peak became asymmetric with a shoulder at higher binding energies. This broadening originates from the appearance of new nitrogen and/or oxygen-containing groups, i.e., C–O/C–N, C=O/N–C=O, and COOH. The formation of carbon- and nitrogen-containing groups further supports the data obtained from XPS survey spectra and FTIR, showing successful implantation of nitrogen and subsequent surface oxidation.

The nitrogen ion implantation was also analysed using N1s high-resolution spectra, shown in Fig. 5d. No significant signals in the N1s region were recorded for the untreated control, while a peak at 399.7 ± 0.5 eV with a high symmetry was recorded for the PBPI^3-treated scaffold, indicative of successful nitrogen ion implantation. The nitrogen implantation process promotes sp^2-hybridised carbon and the formation of an aromatic environment, a mechanism that is supported by the C1 high-resolution data shown in Fig. 5c and our previous studies on PI^3-treatment of 2D polystyrene films [34,48,49]. The aromatic environment serves as a radical reservoir [33,54] as the sp^2-hybridised carbon delocalises and stabilises the unpaired electrons of embedded radicals for the covalent attachment of biomolecules [55].

The uniformity of the optimised surface treatment was assessed by plotting the XPS nitrogen atomic concentrations as a function of position along the length of the scaffolds (Fig. 5e). These results showed a significant increase in atomic nitrogen concentration from 0.1% for the untreated sample to approximately 10.7% for the PBPI^3-treated sample at all locations. Such minimal variations in the atomic nitrogen concentrations provide evidence for homogenous PBPI^3 treatment across the length of the scaffolds, evidence that is also well supported by the FTIR results obtained for the optimal samples (Fig. 4c). This conclusion also correlates well with the homogeneity observed in ToF-SIMS normalised positive counts and associated ion distribution maps, which show a significant decrease in hydrocarbon counts (C_3H_3, C_2H_3, C_4H_3 and C_6H_5) and a significant increase in NH_4 and CH_3O along the entire

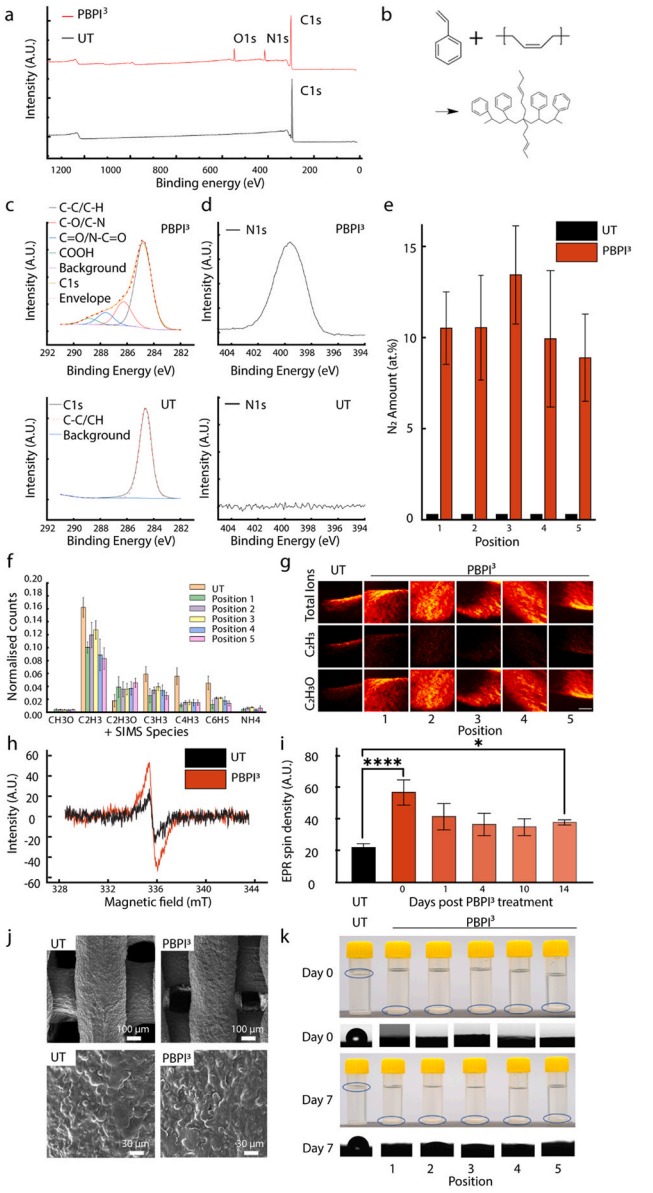

Fig. 5. HiPS scaffolds treated with PBPI^3 at optimised conditions of 8 kV, 3 Torr, 3 kHz, and 20 µs. **a)** XPS survey elemental compositions of untreated and PBPI^3-treated HiPS scaffolds taken from the middle of the assembly [3]. **b)** Chemical structure of untreated HiPS. **c)** XPS C1s high-resolution spectra of untreated and PBPI^3 treated scaffolds (taken at position 3) curve-fitted by four components, C–C/C–H (67.1%), C2: C–O/C–N (18.6%), C3: C=O/N–C=O (9.6%), and COOH (4.8%). **d)** XPS N1s high-resolution spectra of untreated and PBPI^3 treated scaffolds. **e)** Mapped N1s intensity in untreated and PBPI^3-treated scaffolds (n = 5), no significant difference was observed from position 1 to 5). **f)** Mapped positive ion ToF-SIMS spectra of untreated and PBPI^3-treated scaffolds. **g)** ToF-SIMS ion distribution maps of untreated and PBPI^3-treated scaffolds (Total ions, C_2H_3, and C_2H_3O, respectively; scale bar: 100 µm). **h)** EPR intensity for untreated and PBPI^3 scaffolds within 1 h of treatment, indicating unpaired electrons associated with radicals. **i)** EPR spin density as a function of storage time (day 0, 1, 4, 10, and 14 after PBPI^3), suggesting radicals persisted in PBPI^3-treated HiPS scaffolds to enable the covalent bonding of biomolecules. The samples were kept at room temperature in a lab environment with a maximum humidity of 70%. **j)** SEM images at low and high magnifications of untreated and PBPI^3-treated scaffolds taken from the middle position [3] of the assembly. Scale bars are 100 µm and 30 µm as indicated. **k)** Surface wettability qualitative analysis of scaffolds with or without PBPI^3 treatment after being stored in air for 1 h or 7 days. Optical images of the untreated, freshly PBPI^3-treated scaffolds, and 7-day-aged PBPI^3-treated scaffolds placed on MilliQ water, and optical images of water droplets placed on these scaffolds.

scaffolds, regardless of the location of the measurement spots (Fig. 5f and g). These changes in surface chemistry further confirm the occurrence of oxygen and nitrogen and the decrease of hydrocarbon observed in XPS (Fig. 5a). The uniformity of the surface chemistry change was also observed in the ToF-SIMS ion distribution maps.

We have previously reported the capability of surface-embedded radicals for biomolecule immobilisation on 2D surfaces [27,28,31,34,44,53,56–58]. Electron paramagnetic resonance (EPR) was conducted on both untreated and PBPI^3-treated 3D scaffolds from position 3 as a function of time (Fig. 5h and i). At day 0, the freshly PBPI^3-treated scaffolds displayed a significantly higher radical density compared to the untreated control. Fig. 5i further reveals that, following a two-week ageing period at room temperature in the atmosphere, the radicals decayed, yet maintained a higher level compared to the untreated control. Previous research on PIII-treated polystyrene film suggests that this decay can be attributed to the reactive radicals interacting with air [49]. The residual radicals that are embedded deep within the surface can progressively migrate towards the outermost layer of the surface. This migration enables the covalent attachment of biomolecules, a process that can persist even a year post-PBPI^3 treatment [29].

The surface topography of untreated and PBPI^3-treated scaffolds taken from the middle of the assembly (position 3) was evaluated using SEM with representative micrographs shown in Fig. 5j. The SEM images show that PBPI^3 treatment has no visually obvious influence on the topography of the surfaces, suggesting no surface damage occurring at micron level. This physical surface treatment is beneficial as the surfaces are activated without altering their original topography. This is of particular interest because a typically unavoidable limitation of wet-chemistry-based grafting methods involves an essential pre-treatment step using acid/alkali, which can often irreversibly change surface topography and roughness [23]. Such wet-chemistry methods are therefore incompatible with certain MSC expansion platforms, which have specific surface topographies for mechanical regulation of cell adhesion, proliferation, or differentiation [21,59–63].

Surface wettability is another important consideration for cell-contacting materials. Hydrophobic surfaces can irreversibly denature adhered proteins [64,65]. In contrast, hydrophilic surfaces retain the conformation of attached biomolecules, and improve fluid penetration into scaffold pores.

Direct quantification of surface wettability of 3D porous structures using a goniometer poses a significant challenge. Hydrophilic porous surfaces tend to absorb solutions, yielding a reading of 0°, regardless of their level of hydrophilicity, while hydrophobic porous surfaces consistently repel water droplets. Therefore, the surface wettability in the porous scaffolds is often determined by their adsorption behaviour [66]. Here, a goniometer was used to qualitatively evaluate the change of scaffold wettability after PBPI^3 treatment. Fig. 5k shows a water droplet placed on the untreated and PBPI^3-treated scaffolds and imaged after 3.5 s. The water droplet placed on the untreated scaffolds remained on the surface, while that placed on the PBPI^3-treated scaffolds rapidly penetrated the porous structure, indicative of increased hydrophilicity.

This increased hydrophilicity was also confirmed by immersing the scaffolds in MilliQ water. Fig. 5k shows the untreated and freshly PBPI^3-treated scaffolds placed on water. The untreated scaffolds floated, while all PBPI^3-treated scaffolds sank. This observation correlates well with the water absorption of the PBPI^3-treated scaffolds. In contrast, the hydrophobic untreated scaffolds repelled water, leaving air-filled pores that allowed the scaffolds to float. Since scaffold surface topography is unchanged after PBPI^3 treatment, the change in surface chemistry, is likely to be the primary factor underpinning increased wettability. This increase in surface wettability is due to the increase of surface free energy, which results from the polar oxygen-containing groups, such as OH, formed because of surface oxidation as informed by the FTIR and XPS results (Figs. 3–5). Of particular interest is that the PBPI^3-treated scaffolds remained hydrophilic even after one week, as shown in Fig. 5k. This stable hydrophilicity with almost no hydrophobicity recovery is

beneficial for MSC expansion applications as demonstrated in the next sections. Based on all these results together, PBPI^3 treatment was performed at – 8 kV for all the subsequent biology experiments.

3.3. PBPI^3 treatment mediates covalent protein binding to scaffolds

To demonstrate the capacity of scaffolds for covalent protein attachment, untreated and PBPI^3-treated HiPS scaffolds were coated with bovine serum albumin (BSA) as a model protein and were subjected to stringent SDS detergent washing to remove physisorbed molecules (Fig. 6a). Before detergent washing, comparable amounts of protein were detected on both untreated and PBPI^3-treated scaffolds. After washing, protein levels were negligible on the untreated scaffolds but remained unchanged on the PBPI^3-treated materials. This retention of BSA on PBPI^3-treated scaffolds suggests that most protein molecules were covalently attached to the PBPI^3-treated scaffold surface.

Covalent protein immobilisation to PBPI^3-treated scaffolds was similarly observed via fluorescent detection of a Cy5-conjugated antibody coated on control and treated constructs (Fig. 6b). Before washing with a non-ionic detergent, Tween-20, fluorescent protein signals were detected on both untreated and treated scaffolds. Fluorescence on the untreated scaffolds appeared brighter than that on the treated scaffolds, suggesting that either more antibody molecules are bound to the untreated surface, and/or that the conformation of bound proteins differs between the untreated and treated constructs. Hydrophobic surfaces, such as the untreated scaffolds, are known to induce a conformational change of adhered molecules via increased hydrophobic interactions [23,24] which may lead to increased protein adsorption via aggregation. After Tween-20 washing, protein fluorescence was visibly dampened on the untreated scaffolds, indicating loss of majority of the surface-bound antibodies. In contrast, while fluorescence may appear decreased on the treated materials due to the removal of physisorbed antibodies, these signals were largely retained across the entire surface of the treated materials, corresponding to the presence of stably-bound proteins. These results consistently support the covalent immobilisation of proteins on the PBPI^3-treated scaffolds.

To prime the scaffolds for MSC culture, they were coated with fibroblast growth factor 2 (FGF2), a potent mitogenic agent known to promote early-passage MSC proliferation and to preserve MSC differentiation potential [67–70]. In line with previous observations, similar levels of FGF2 were initially present on both untreated and PBPI^3-treated constructs (Fig. 6c). However, following washing in 2% (v/v) Tween-20, FGF2 levels on untreated controls were reduced by 81 ± 9% due to the removal of weakly physisorbed protein molecules. In contrast, FGF2 levels on PBPI^3-treated scaffolds were preserved, demonstrating stable protein adhesion indicative of covalent linkages between FGF2 molecules and the reactive polymer surface. Covalent bio-functionalisation minimises the Vroman effect, i.e. the exchange of physisorbed proteins with non-target proteins that possess a higher affinity for the material surface, therefore providing a stable instructive interface for seeded cells [24].

To further characterise concentration-dependent FGF2 adhesion on scaffolds, the amount of surface-bound FGF2 at each coating concentration was detected via ELISA (Fig. 6d). FGF2 adhesion on PBPI^3-treated scaffolds was higher than that on untreated scaffolds over multiple concentrations. At lower FGF2 coating concentrations (10 and 20 ng/mL), PBPI^3-treated scaffolds supported 135 ± 4% and 221 ± 46% increased binding compared to untreated scaffolds, demonstrating significantly improved biomolecule capture and attachment efficiency. As shown in the next section, these low FGF2 coating concentrations were sufficient to elicit a maximal cell proliferative response on the treated scaffolds. This result has an important implication as it indicates that PBPI^3 treatment lowers the protein concentration necessary for functional coverage of scaffolds, reducing the cost of surface

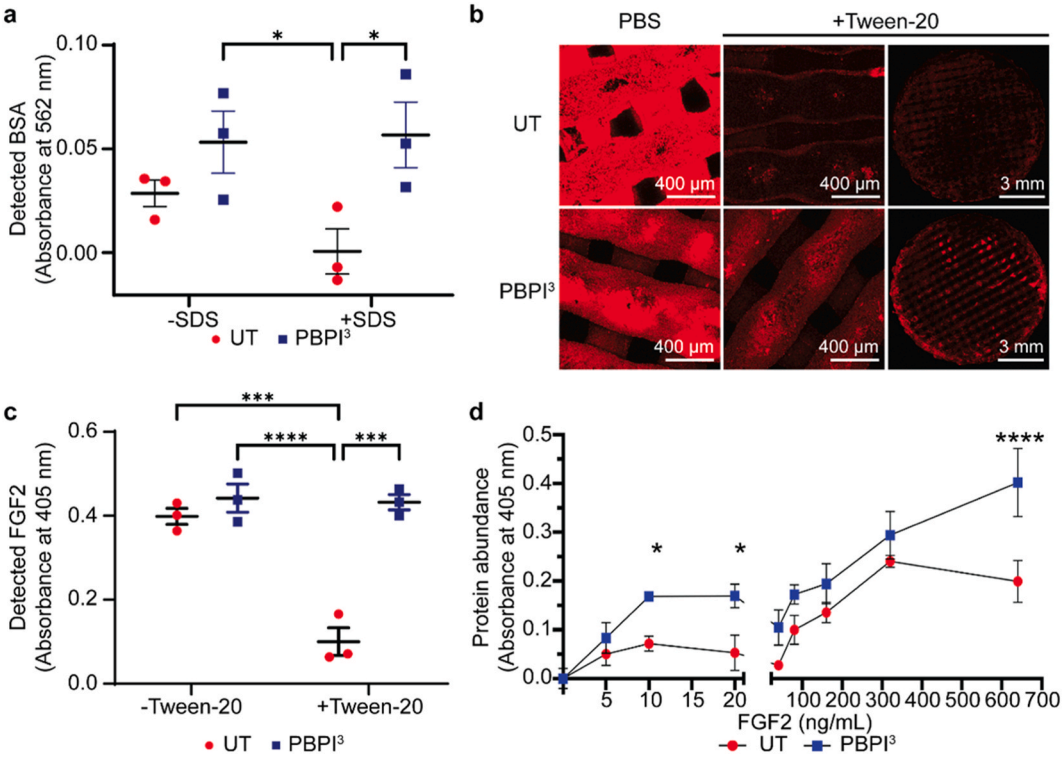

Fig. 6. a) Quantification of surface-bound bovine serum albumin (BSA) on untreated and PBPI^3-treated scaffolds with and without SDS washing via a BCA assay. b) Fluorescent images of Cy5-conjugated antibody coated on untreated and PBPI^3-treated scaffolds before and after Tween-20 washing. Scale bars are 400 µm or 3 mm as indicated. c) Antibody detection of surface-bound fibroblast growth factor 2 (FGF2) on untreated and PBPI^3-treated scaffolds before and after Tween-20 washing. d) Antibody detection of surface-bound FGF2 on untreated and PBPI^3-treated scaffolds after being coated with 0–640 ng/mL of FGF2. (*$p < 0.05$; ***$p < 0.001$; ****$p < 0.0001$).

functionalisation.

FGF2 is typically added into the cell culture medium as a soluble supplement rather than coated onto the culture substrate. However, since FGF2 is relatively unstable and prone to degradation in solution [71–73], many efforts have been made to stabilise FGF2 on culture surfaces. Current approaches have relied on decorating surfaces with intermediary molecules such as heparin, or fusing FGF2 with linker sequences, such as maltose binding protein or a His-tag, to bind and present the growth factor [73–75]. In contrast, PBPI^3-treated scaffolds enable direct, one-step immobilisation of FGF2. This process is rapid, scalable, and does not require additional engineering of the target protein.

3.4. PBPI^3-treated, FGF2-functionalised scaffolds significantly promote MSC proliferation

Following successful FGF2 immobilisation on the scaffolds, the functional presentation of the surface-bound growth factor must be determined. Protein orientation is not typically an issue with indirect or linker-mediated immobilisation approaches, as the intermediary or linker moieties can guide binding conformation. However, with direct immobilisation techniques, the adhered protein may be in a non-native conformation in which its cell-interactive sites are disrupted or inaccessible [35,76].

To confirm the functionality of the surface-bound FGF2 molecules, MSCs were first cultured on untreated and PI^3-treated 2D polystyrene films coated with increasing concentrations of FGF2 (Fig. 7a-c). On untreated films, a minimum FGF2 coating concentration of 20 ng/mL was required to increase MSC proliferation compared to the uncoated controls. Interestingly, supplementation of FGF2 in the culture medium alone failed to promote MSC growth on the bare untreated films (Fig. 7a). On PI^3-treated films, a lower FGF2 coating concentration of 10 ng/mL was sufficient to significantly improve MSC expansion compared to the uncoated surfaces. The extent of this benefit surpassed that observed with FGF2 supplementation of culture media (Fig. 7b). Interestingly, as the concentration of immobilised FGF2 increased to 500–1000 ng/mL, this beneficial effect was not observed, potentially due to the complete masking of the cell-adhesive plasma-modified substrate. Maximal MSC proliferation appears to require a balance between cell exposure to the mitogenic FGF2 signals and the underlying cell attachment substrate, which was optimal at lower coating concentrations of FGF2.

To demonstrate another key benefit of PI^3-mediated FGF2 surface functionalisation, MSCs grown for 7 days on untreated and treated films coated with varying FGF2 concentrations were washed and stained (Fig. 7c). Cells on untreated films with <100 ng/mL FGF2 were easily lost to delamination. In contrast, cell delamination did not occur on all PI^3-treated films, demonstrating the stability of the covalently linked bioactive FGF2 coating over the duration of the MSC expansion period.

Taken together, these findings demonstrated that FGF2 retained pro-proliferative functionality when adhered to surfaces, and is at least comparable in efficacy to FGF2 supplemented in solution. In addition, PBPI^3 treatment reduces the FGF2 coating concentration required to achieve the maximum biological benefit, consistent with previous ELISA observations of enhanced biomolecule attachment on treated scaffolds.

To translate the technology from 2D surfaces to 3D scaffolds, an initial cell compatibility test was performed with bare scaffolds. Both untreated and PBPI^3-treated scaffolds, without FGF2 coating, were also shown to be non-cytotoxic. MSCs cultured over 10 days in media incubated with untreated or PBPI^3-treated scaffolds showed 87 ± 1% and 89 ± 2% cell viability, respectively, relative to cells grown in fresh media (Fig. S2).

Untreated and PBPI^3-treated 3D scaffolds, coated with a range of FGF2 concentrations, supported similar MSC proliferation profiles as those observed on the 2D films (Fig. 7d-f). At 14 days post-seeding, MSC growth was present only on untreated scaffolds coated with higher (≥160 ng/mL) concentrations of FGF2, but was abundant on all PBPI^3-treated scaffolds, particularly those functionalised with lower (10–20 ng/mL) amounts of FGF2 (Fig. 7d). To further characterise these findings, cell growth over 16 days was measured via metabolic activity and compared among bare or FGF2-coated untreated and PBPI^3-treated scaffolds. MSC numbers on untreated scaffolds were significantly increased upon substrate coating with 20 ng/mL FGF2 at day 10, and with 200 ng/mL FGF2 at days 10 and 12 (Fig. 7e). However, MSCs on PBPI^3-treated scaffolds proliferated to the highest extent following substrate coating with a low concentration of FGF2 (Fig. 7f). By day 14, MSC numbers were significantly higher on 20 ng/mL FGF2-coated PBPI^3-treated scaffolds, compared to those on the bare PBPI^3-treated scaffolds, or PBPI^3-treated scaffolds coated with higher FGF2 concentrations. Consequently, FGF2 concentrations of 10–20 ng/mL were considered to be the optimally effective concentrations for subsequent scaffold bio-functionalisation. It again supported the previous observations on plasma-treated 2D films, and suggested there is a fine balance between the display of PI3-treated surface and growth factor required for maximal benefit for MSC.

The suitability of optimally functionalised scaffolds as an MSC expansion platform was further characterised by assessing cell yield, metabolic activity and phenotype at multiple timepoints over 14 days (Fig. 8). PBPI^3 treatment alone, even in the absence of additional biomolecules, significantly improved cell adhesion and growth on the scaffolds. This was demonstrated by the increased cell abundance on bare PBPI^3-treated scaffolds (PBPI^3 0) compared to that on bare untreated scaffolds (UT 0), which was observed even at an early timepoint of 3 days post-seeding, and which persisted until 14 days post-seeding (Fig. 8a). By day 14, bare PBPI^3-treated scaffolds increased MSC numbers by 6.8 ± 0.9 fold compared to untreated controls (Fig. 8a).

Functionalisation with FGF2 amplifies the proliferative benefits of PBPI^3 treatment. FGF2-coated, PBPI^3-treated scaffolds further improved MSC proliferation by 1.5 ± 0.1 fold over bare PBPI^3-treated materials and by 9.8 ± 0.6 fold compared to untreated controls.

In line with these results, representative images of MSCs cultured on untreated scaffolds showed minimal cell adhesion and proliferation over 14 days, regardless of FGF2 presence (Fig. 8b). While all PBPI^3-treated scaffolds promoted increasingly confluent MSC growth over the same period, the highest cell densities by day 14 were observed on the PBPI^3-treated and FGF2-coated materials, in line with the quantitative results (Fig. 8a). Surface modification via PBPI^3 activation and FGF2 functionalisation clearly improves the capacity of the 3D scaffolds for directing MSC expansion.

These scaffolds present a cost-effective strategy for the *ex vivo* propagation of MSCs. They were coated with 20 ng/mL FGF2, which is in line with FGF2 concentrations commonly used for media supplementation [69,77–79]. While FGF2 in solution needs to be replenished with every media change, the substrate-immobilised FGF2 represents a beneficial one-off cost as it remains stable over the duration of the cell proliferative cycle and requires no replenishment. Usage savings will escalate with longer expansion times and higher volumes of culture media. FGF2 usage is estimated to be reduced by at least 50% for cells grown on 2D films for 7 days, and up to 70% for cells cultured in 3D scaffolds for 14 days.

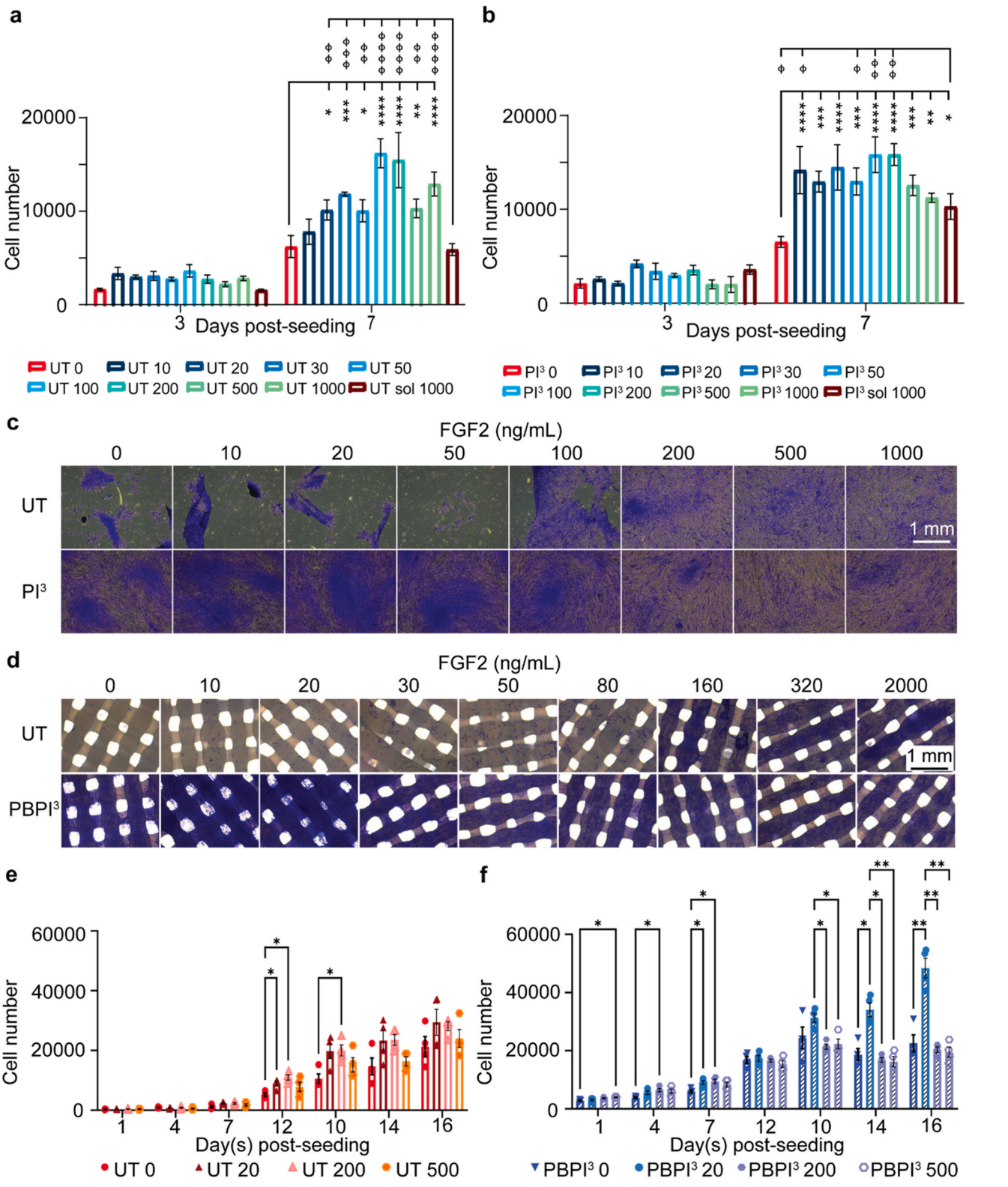

Fig. 7. MSC proliferation over 7 days on **a)** Untreated (UT) or **b)** PI^3-treated 2D polystyrene films coated with 0–1000 ng/mL FGF2, or with 1000 ng/mL FGF2 supplemented in culture medium. Cell numbers were measured by DNA quantification at 4- and 7-days post-seeding. The asterisk (*) symbol denotes statistical comparison with the no-FGF2 control (UT 0 or PI^3 0); *$p < 0.05$; **$p < 0.01$; ***$p < 0.001$; ****$p < 0.0001$. The phi (Φ) symbol represents statistical comparison with FGF2 in solution conditions (UT sol 1000 or PI^3 sol 1000); Φ $p < 0.05$; Φ Φ $p < 0.01$; Φ Φ Φ $p < 0.001$; Φ Φ Φ Φ $p < 0.0001$. **c)** Representative images of crystal violet stained MSCs cultured for 7 days on untreated and PI^3-treated films coated with 0–1000 ng/mL FGF2. Scale bar: 1 mm. **d)** Representative images of crystal violet stained MSCs cultured for 14 days on untreated and $PBPI^3$-treated 3D scaffolds coated with 0–2000 ng/mL FGF2. Scale bar: 1 mm. **e-f)** Cell numbers determined from metabolic activity as measured with Alamar Blue assay. Cells were grown on **e)** untreated scaffolds or **f)** $PBPI^{3-}$treated scaffolds, with or without FGF2 coating at 20, 200, and 500 ng/mL.

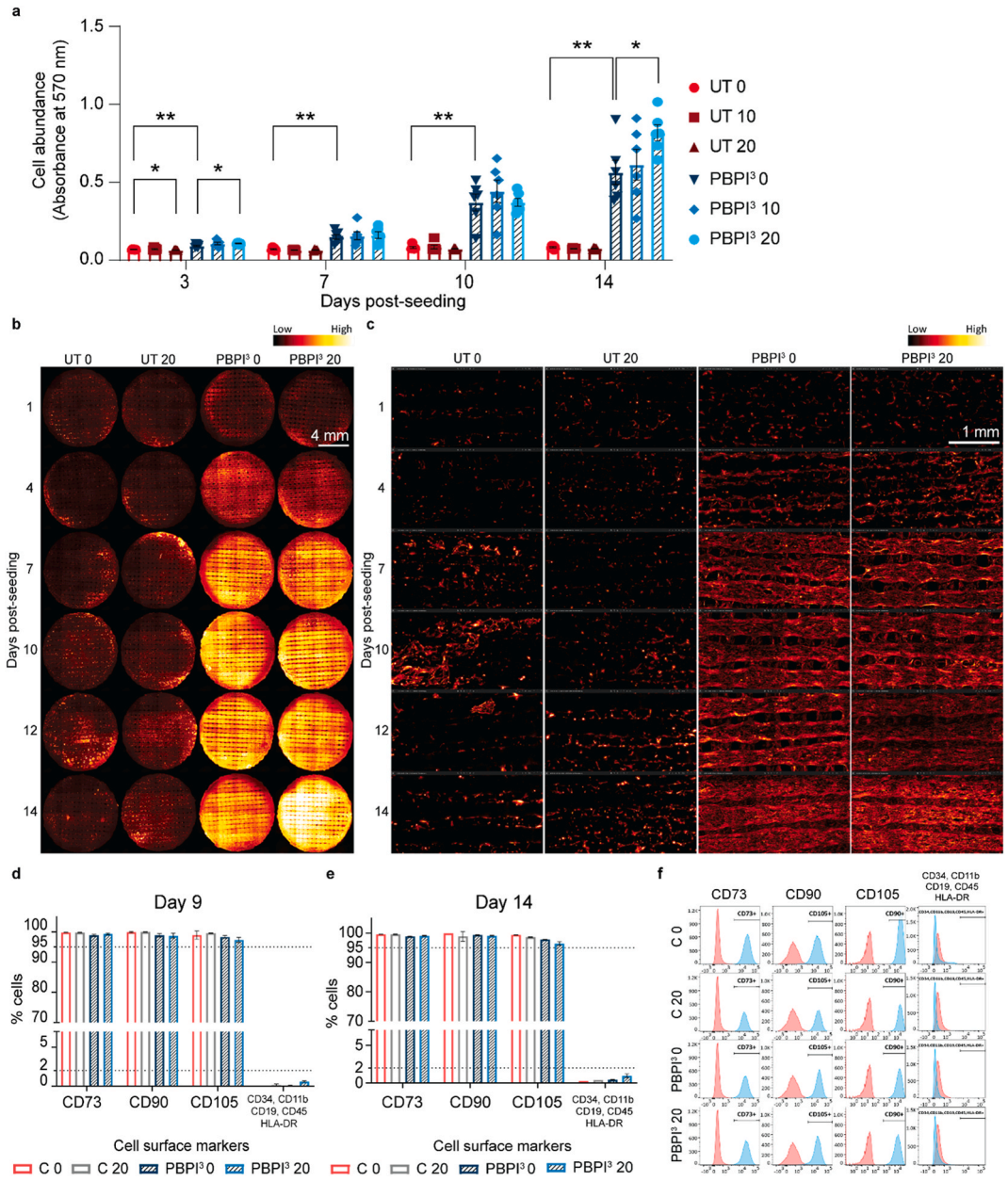

Fig. 8. MSC proliferation and phenotype changes over 14 days on 3D scaffolds with or without PBPI^3 surface modification and FGF2 functionalisation. **a)** Cell abundance on untreated and PBPI^3-treated scaffolds coated with 0, 10, or 20 ng/mL FGF2 at 3-, 7-, 10- and 14-days post-seeding (*$p < 0.05$). **b-c)** Fluorescent images of MSCs, stained for f-actin (red) on untreated and treated scaffolds with or without 20 ng/mL FGF2, at 1, 4, 7, 10, 12 and 14 days post-seeding. Fluorescent intensity, as a measure of cell abundance, is depicted by a LUT colour scale from black (low), red (medium), to yellow (high). Images were taken **b)** across the whole scaffold (scale bar: 4 mm). and **c)** with magnified snapshots provided (scale bar: 1 mm). **d-f)** Surface marker expression of MSCs expanded on tissue culture plastic (C), or on PBPI^3-treated HiPS scaffolds with or without functionalisation with 20 ng/mL FGF2. The percentage of cells that express CD73, CD105, CD90 and hematopoietic lineage markers CD34, CD11b, CD19, CD45, HLA-DR at **d)** day 9, and **e)** day 14 post-seeding are shown. **f)** Representative surface marker expression profiles of MSC populations grown on various substrates for 14 days. Cell samples are shown in blue, while isotype controls are in red. Gatings used to quantify marker expression are also indicated.

3.5. MSCs expanded on PBPI^3-treated and FGF2-coated scaffolds retain their phenotype

The phenotypic preservation of MSCs harvested after culture is an essential consideration for stem cell expansion platforms. To meet the criteria for MSC validation as set by the International Society for Cell Therapy, >95% of the cell population must express the MSC surface markers CD73, CD90 and CD105, while <2% must express the hematopoietic stem cell surface molecules CD34, CD45, CD11b or CD14, CD19 or CD79α, and HLA-DR [80,81].

MSCs grown on PBPI^3-treated scaffolds with or without FGF2 retained characteristic cell surface marker expression, similarly to positive control cells that were regularly passaged on tissue culture plastic with or without FGF2 coating (Fig. 8d–f). The functionalised scaffolds promoted cell proliferation without compromising MSC stemness, as demonstrated by >96% of cells expressing all three MSC markers and <1% of cells expressing lineage-negative markers at 9 and 14 days post-seeding.

To further confirm their multipotent capability, the expanded MSCs were analysed for transcriptional expression of Oct4, a transcription factor associated with MSC proliferation and multi-lineage differentiation [82]. Oct4 expression of cells cultured for 14 days on PBPI^3-treated

and FGF2 biofunctionalised scaffolds (PBPI^3 20) were compared against cells grown on bare PBPI^3 scaffolds (PBPI^3 0), and cells regularly passaged on TCP (C 0) or TCP coated with FGF2 (C 20). Consistent with the maintenance of MSC surface marker expression, cells cultured in all conditions expressed comparable levels of Oct4 expression (Fig. S3). This finding provides further functional validation of the MSCs harvested from the functionalised 3D scaffolds, and demonstrates the capacity of PBPI^3-treated and FGF2-functionalised scaffolds to promote MSC expansion while robustly preserving cell quality and stemness for downstream applications.

This scaffold technology is scalable for large-scale cell expansion. The use of simple extrusion-based 3D printing technology enables efficient and cost-effective fabrication of the scaffolds, which can be made of low-cost synthetic materials to increase accessibility for large-scale production. This approach ensures the potential for widespread implementation in various research and industrial settings. This plasma ignition method offers a flexible approach for adapting different plasma treatment procedures, making it possible to handle scaffolds of varying material compositions, pore designs, and geometrical structures to meet specific application needs. Crucially, this technique can be harnessed to introduce functional groups that can either directly modulate cellular activity or immobilise biomolecules to influence cellular behaviour [57]. These scaffolds can be integrated into large bioreactor systems that automate the protein functionalisation of scaffold surfaces and subsequent cell culture processes, including cell seeding, media changes, and cell harvest. The large pores within the scaffold allow efficient nutrient and gas exchange, and promote cell colonisation, growth and extraction. Additionally, cell harvesting can be achieved using conventional enzymatic dissociation using trypsin. Furthermore, there is scope to incorporate combinations of cell-instructive biomolecules within the scaffold, providing a more comprehensive and tailored culture environment. The PBPI^3 approach also allows for the surface immobilisation of other labile components in the culture medium, potentially reducing further the reagent costs associated with cell production. However, certain limitations still exist, as is the case with other large-scale expansion systems. The shear stress imposed on the cells within bioreactor systems needs to be carefully managed to prevent any adverse effects on cell viability and function. Additionally, the plasma-treated scaffold surfaces cannot be functionalised with biomolecules that need to be internalised by cells for biological signalling to occur.

Applications for this technology reach beyond stem cell expansion. The ability to produce homogeneously cell-instructive biofunctionalised surfaces inside 3D porous constructs, using PBPI^3 as a cleaner, safer, and faster alternative to wet chemistry-based linker methods, paves the way towards the development of compositionally diverse and functionally versatile 3D materials for next-generation cell- or protein-based applications, such as implants, personalised drug testing platforms, and lab-on-chip systems. For example, MSCs can be immobilised within the scaffolds to serve as cell factories for secreting cytokines, growth factors, extracellular matrix components, or extracellular vesicles. Indeed, hollow fibre systems have similarly been used for the mass production of antibodies [83] or extracellular vesicles [84]. Additionally, the plasma technology may be adapted to modify scaffold surfaces with antibodies to capture and detect circulating cells *in vivo*, such as circulating tumour cells, for disease diagnosis and monitoring [85]. Extending beyond the biomedical space, the versatility of this PBPI^3 technology lends itself to diverse applications such as membranes for filtration, and porous columns and fluidised beds for purification, separation, and catalysis.

4. Conclusions

This paper reports the development of a bioactive, micrometre-sized porous 3D scaffold adapted for stem cell expansion. Harnessing a breakthrough plasma-based technology, referred to as PBPI^3, homogenous surface treatment of porous scaffolds is achieved. The PBPI^3-treated 3D scaffolds mediate the direct, stable, and functional surface binding of cell-modulatory molecules, including those typically replenished in solution such as FGF2. The functionalised scaffolds significantly promote MSC proliferation while retaining stemness, resulting in higher expansion efficacies at a reduced cost.

The ability to produce homogeneously biofunctionalised surfaces inside scaffolds will bring significant potential to substitute the current wet-chemistry-based biofunctionalisation methods for tissue engineering. This new technology paves the way towards the development of compositionally diverse and functionally versatile 3D porous constructs, including next-generation stem cell instructive materials.

Credit author statement

Anyu Zhang: Methodology, Investigation, Formal analysis, Software, Writing – original draft, **Johnny Kuan Un Wong**: Methodology, Investigation, Formal analysis, Software, Writing – original draft, **Katazhyna Redzikultsava**: Investigation, **Mark Baldry**: Investigation, **Seyedeh KH Alavi**: Investigation, **Ziyu Wang**: Investigation, **Eveline van Koten**: Investigation, **Anthony Weiss**: Resources, **Marcela Bilek**: Conceptualisation, Writing – review & editing, Funding acquisition, Supervision, **Giselle C. Yeo**: Conceptualization, Writing – review & editing, Funding acquisition, Supervision, Project administration, **Behnam Akhavan**: Conceptualization, Writing – review & editing, Funding acquisition, Supervision, Project administration.

Declaration of competing interest

The authors declare that they have no known competing financial interests or personal relationships that could have appeared to influence the work reported in this paper.

Data availability

Data will be made available on request.

Acknowledgements

The authors gratefully acknowledge funding from the Australian Research Council (DP190103507, FL190100216, DE210100662, and DP220101644), and National Health and Medical Research Council (2017233). The authors acknowledge the technical and scientific assistance of Dr Ying Ying Su, Dr Pamela Young and Sydney Microscopy & Microanalysis, the University of Sydney node of Microscopy Australia. The authors acknowledge the Sydney Cytometry Core Research Facility, a joint initiative of Centenary Institute and the University of Sydney, for assistance with flow cytometry. The authors acknowledge the technical and scientific assistance of Michelle Wood, Sydney Analytical - Vibrational Spectroscopy, Core Research Facilities, and the Sydney Nanoscience Hub. The authors acknowledge the technical services of Dr Tino Kausmann and the School of Chemical and Biomolecular Engineering. The authors acknowledge the technical and scientific advice and assistance of Dr Aaron Gilmour and the technical support of Bingyan Liu and Yuan Cheng.

Appendix A. Supplementary data

Supplementary data to this article can be found online at https://doi.org/10.1016/j.mtbio.2023.100727.

References

[1] M.F. Pittenger, A.M. Mackay, S.C. Beck, R.K. Jaiswal, R. Douglas, J.D. Mosca, et al., Multilineage potential of adult human mesenchymal stem cells, Science 284 (5411) (1999) 143–147.

[2] Y. Jiang, B.N. Jahagirdar, R.L. Reinhardt, R.E. Schwartz, C.D. Keene, X.R. Ortiz-Gonzalez, et al., Pluripotency of mesenchymal stem cells derived from adult marrow, Nature 418 (6893) (2002) 41–49.

[3] B. Amorin, A.P. Alegretti, V. Valim, A. Pezzi, A.M. Laureano, M.A.L. da Silva, et al., Mesenchymal stem cell therapy and acute graft-versus-host disease: a review, Hum. Cell 27 (4) (2014) 137–150.

[4] K. Le Blanc, F. Frassoni, L. Ball, F. Locatelli, H. Roelofs, I. Lewis, et al., Mesenchymal stem cells for treatment of steroid-resistant, severe, acute graft-versus-host disease: a phase II study, Lancet 371 (9624) (2008) 1579–1586.

[5] R. Soler, L. Orozco, A. Munar, M. Huguet, R. López, J. Vives, et al., Final results of a phase I–II trial using ex vivo expanded autologous mesenchymal stromal cells for the treatment of osteoarthritis of the knee confirming safety and suggesting cartilage regeneration, Knee 23 (4) (2016) 647–654.

[6] W.S. Lee, H.J. Kim, K.I. Kim, G.B. Kim, W. Jin, Intra-articular injection of autologous adipose tissue-derived mesenchymal stem cells for the treatment of knee osteoarthritis: a phase IIb, randomized, placebo-controlled clinical trial, Stem Cells Transl. Med. 8 (6) (2019) 504–511.

[7] G.M. Ellison-Hughes, L. Colley, K.A. O'Brien, K.A. Roberts, T.A. Agbaedeng, M. D. Ross, The role of MSC therapy in attenuating the damaging effects of the cytokine storm induced by COVID-19 on the heart and cardiovascular system, Front. Cardiovasc. Med. 7 (2020) 327.

[8] A. Kadner, S.P. Hoerstrup, G. Zund, K. Eid, C. Maurus, S. Melnitchouk, et al., A new source for cardiovascular tissue engineering: human bone marrow stromal cells, Eur. J. Cardio. Thorac. Surg. 21 (6) (2002) 1055–1060.

[9] D.G. Phinney, D.J. Prockop, Concise review: mesenchymal stem/multipotent stromal cells: the state of transdifferentiation and modes of tissue repair—current views, Stem Cell. 25 (11) (2007) 2896–2902.

[10] A.C. Yorukoglu, A. Kiter, S. Akkaya, N.L. Satiroglu-Tufan, A.C. Tufan, A concise review on the use of mesenchymal stem cells in cell sheet-based tissue engineering with special emphasis on bone tissue regeneration, Stem Cell. Int. 2017 (2017).

[11] A.R. Tan, C.T. Hung, Concise review: mesenchymal stem cells for functional cartilage tissue engineering: taking cues from chondrocyte-based constructs, Stem Cells Transl. Med. 6 (4) (2017) 1295–1303.

[12] A. Augello, C. De Bari, The regulation of differentiation in mesenchymal stem cells, Hum. Gene Ther. 21 (10) (2010) 1226–1238.

[13] B. Koh, N. Sulaiman, M.B. Fauzi, J.X. Law, M.H. Ng, R.B.H. Idrus, et al., Three dimensional microcarrier system in mesenchymal stem cell culture: a systematic review, Cell Biosci. 10 (2020) 1–16.

[14] W. Wagner, P. Horn, M. Castoldi, A. Diehlmann, S. Bork, R. Saffrich, et al., Replicative senescence of mesenchymal stem cells: a continuous and organized process, PLoS One 3 (5) (2008), e2213.

[15] M. António, A. Fernandes-Platzgummer, C.L. da Silva, J.M. Cabral, Scalable microcarrier-based manufacturing of mesenchymal stem/stromal cells, J. Biotechnol. 236 (2016) 88–109.

[16] P. Zheng, Q. Yao, F. Mao, N. Liu, Y. Xu, B. Wei, et al., Adhesion, proliferation and osteogenic differentiation of mesenchymal stem cells in 3D printed poly-ε-caprolactone/hydroxyapatite scaffolds combined with bone marrow clots, Mol. Med. Rep. 16 (4) (2017) 5078–5084.

[17] L. Vymetalova, T. Kucirkova, L. Knopfova, V. Pospisilova, T. Kasko, H. Lejdarova, et al., Large-scale automated hollow-fiber bioreactor expansion of umbilical cord-derived human mesenchymal stromal cells for neurological disorders, Neurochem. Res. 45 (1) (2020) 204–214.

[18] A. Rashad, S. Mohamed-Ahmed, M. Ojansivu, K. Berstad, M.A. Yassin, T. Kivijarvi, et al., Coating 3D printed polycaprolactone scaffolds with nanocellulose promotes growth and differentiation of mesenchymal stem cells, Biomacromolecules 19 (11) (2018) 4307–4319.

[19] T.L. Jenkins, D. Little, Synthetic scaffolds for musculoskeletal tissue engineering: cellular responses to fiber parameters, NPJ Regenerative Med. 4 (1) (2019) 1–14.

[20] A. Dulgar-Tulloch, R. Bizios, R. Siegel, Human mesenchymal stem cell adhesion and proliferation in response to ceramic chemistry and nanoscale topography, J. Biomed. Mater. Res. Part A 90 (2) (2009) 586–594.

[21] S.J. Heo, S.E. Szczesny, D.H. Kim, K.S. Saleh, R.L. Mauck, Expansion of mesenchymal stem cells on electrospun scaffolds maintains stemness, mechano-responsivity, and differentiation potential, J. Orthop. Res. 36 (2) (2018) 808–815.

[22] X.D. Chen, Extracellular matrix provides an optimal niche for the maintenance and propagation of mesenchymal stem cells, Birth Defects Res. Part C Embryo Today - Rev. 90 (1) (2010) 45–54.

[23] C. Stewart, B. Akhavan, S.G. Wise, M.M. Bilek, A review of biomimetic surface functionalization for bone-integrating orthopedic implants: mechanisms, current approaches, and future directions, Prog. Mater. Sci. 106 (2019), 100588.

[24] S.L. Hirsh, D.R. McKenzie, N.J. Nosworthy, J.A. Denman, O.U. Sezerman, M. M. Bilek, The Vroman effect: competitive protein exchange with dynamic multilayer protein aggregates, Colloids Surf. B Biointerfaces 103 (2013) 395–404.

[25] C.A. Tannoury, H.S. An, Complications with the use of bone morphogenetic protein 2 (BMP-2) in spine surgery, Spine J. 14 (3) (2014) 552–559.

[26] K. Schmidt-Bleek, B.M. Willie, P. Schwabe, P. Seemann, G.N. Duda, BMPs in bone regeneration: less is more effective, a paradigm-shift, Cytokine Growth Factor Rev. 27 (2016) 141–148.

[27] R. Walia, B. Akhavan, E. Kosobrodova, A. Kondyurin, F. Oveissi, S. Naficy, et al., Hydrogel– solid hybrid materials for biomedical applications enabled by surface-embedded radicals, Adv. Funct. Mater. 30 (38) (2020), 2004599.

[28] M.M. Bilek, D.R. McKenzie, Plasma modified surfaces for covalent immobilization of functional biomolecules in the absence of chemical linkers: towards better biosensors and a new generation of medical implants, Biophys. Rev. 2 (2) (2010) 55–65.

[29] M.M. Bilek, D.V. Bax, A. Kondyurin, Y. Yin, N.J. Nosworthy, K. Fisher, et al., Free radical functionalization of surfaces to prevent adverse responses to biomedical devices, Proc. Natl. Acad. Sci. USA 108 (35) (2011) 14405–14410.

[30] K. Lau, A. Waterhouse, B. Akhavan, L. Gao, H.N. Kim, F. Tang, et al., Biomimetic silk biomaterials: perlecan-functionalized silk fibroin for use in blood-contacting devices, Acta Biomater.132 (2021) 162–175.

[31] A. Kondyurin, K. Lau, F. Tang, B. Akhavan, W. Chrzanowski, M.S. Lord, et al., Plasma ion implantation of silk biomaterials enabling direct covalent immobilization of bioactive agents for enhanced cellular responses, ACS Appl. Mater. Interfaces 10 (21) (2018) 17605–17616.

[32] X. Cheng, J. Fei, A. Kondyurin, K. Fu, L. Ye, M.M. Bilek, et al., Enhanced biocompatibility of polyurethane-type shape memory polymers modified by plasma immersion ion implantation treatment and collagen coating: an in vivo study, Mater. Sci. Eng. C 99 (2019) 863–874.

[33] M.M.M. Bilek, A. Kondyurin, S. Dekker, B.C. Steel, R.A. Wilhelm, R. Heller, et al., Depth-resolved structural and compositional characterization of ion-implanted polystyrene that enables direct covalent immobilization of biomolecules, J. Phys. Chem. C 119 (29) (2015) 16793–16803.

[34] E.A. Wakelin, M.J. Davies, M.M. Bilek, D.R. McKenzie, Temperature activated diffusion of radicals through ion implanted polymers, ACS Appl. Mater. Interfaces 7 (47) (2015) 26340–26345.

[35] L.J. Martin, B. Akhavan, M.M. Bilek, Electric fields control the orientation of peptides irreversibly immobilized on radical-functionalized surfaces, Nat. Commun. 9 (1) (2018) 1–11.

[36] M.L. Steen, A.C. Jordan, E.R. Fisher, Hydrophilic modification of polymeric membranes by low temperature H2O plasma treatment, J. Membr. Sci. 204 (1–2) (2002) 341–357.

[37] L. Huang, J.T. Arena, J.R. McCutcheon, Surface modified PVDF nanofiber supported thin film composite membranes for forward osmosis, J. Membr. Sci. 499 (2016) 352–360.

[38] C. Wang, Y. Ren, Y. Qiu, Penetration depth of atmospheric pressure plasma surface modification into multiple layers of polyester fabrics, Surf. Coating. Technol. 202 (1) (2007) 77–83.

[39] A. Pegalajar-Jurado, M.N. Mann, M.R. Maynard, E.R. Fisher, Hydrophilic modification of polysulfone ultrafiltration membranes by low temperature water vapor plasma treatment to enhance performance, Plasma Process. Polym. 13 (6) (2016) 598–610.

[40] M. Zelzer, D. Scurr, B. Abdullah, A.J. Urquhart, N. Gadegaard, J.W. Bradley, et al., Influence of the plasma sheath on plasma polymer deposition in advance of a mask and down pores, J. Phys. Chem. B 113 (25) (2009) 8487–8494.

[41] E. Sardella, R.A. Salama, G.H. Waly, A.N. Habib, P. Favia, R. Gristina, Improving internal cell colonization of porous scaffolds with chemical gradients produced by plasma assisted approaches, ACS Appl. Mater. Interfaces 9 (5) (2017) 4966–4975.

[42] P. Cools, C. Mota, I. Lorenzo-Moldero, R. Ghobeira, N. De Geyter, L. Moroni, et al., Acrylic acid plasma coated 3D scaffolds for cartilage tissue engineering applications, Sci. Rep. 8 (1) (2018) 1–15.

[43] L. Safinia, N. Datan, M. Höhse, A. Mantalaris, A. Bismarck, Towards a methodology for the effective surface modification of porous polymer scaffolds, Biomaterials 26 (36) (2005) 7537–7547.

[44] G.A. Katsifis, N. Suchowerska, D.R. McKenzie, Quantification of dose in plasma immersion ion implantation of polymer bone scaffolds: probe diagnostics of a pulsed dielectric barrier discharge, Plasma Process. Polym. 17 (12) (2020), 2000113.

[45] M. Croes, B. Akhavan, O. Sharifahmadian, H. Fan, R. Mertens, R.P. Tan, et al., A multifaceted biomimetic interface to improve the longevity of orthopedic implants, Acta Biomater. 110 (2020) 266–279.

[46] E. Kosobrodova, A. Kondyurin, V. Solodko, A.S. Weiss, D.R. McKenzie, M.M. Bilek, Covalent biofunctionalization of the inner surfaces of a hollow-fiber capillary bundle using packed-bed plasma ion implantation, ACS Appl. Mater. Interfaces 12 (28) (2020) 32163–32174.

[47] K. Redzikultsava, M. Baldry, A. Zhang, S.K. Alavi, B. Akhavan, M.M. Bilek, Cold plasma treatment of porous scaffolds: design principles, Plasma Process. Polym. 19 (7) (2022), 2200018.

[48] E.A. Kosobrodova, A.V. Kondyurin, K. Fisher, W. Moeller, D.R. McKenzie, M. M. Bilek, Free radical kinetics in a plasma immersion ion implanted polystyrene: theory and experiment, Nucl. Instrum. Methods Phys. Res. Sect. B Beam Interact. Mater. Atoms 280 (2012) 26–35.

[49] E. Kosobrodova, A. Kondyurin, D. McKenzie, M. Bilek, Kinetics of post-treatment structural transformations of nitrogen plasma ion immersion implanted polystyrene, Nucl. Instrum. Methods Phys. Res. Sect. B Beam Interact. Mater. Atoms 304 (2013) 57–66.

[50] Y. Li, D.-Z. Yang, J.-J. Qiao, L. Zhang, W.-Z. Wang, Z.-L. Zhao, et al., The dynamic evolution and interaction with dielectric material of the discharge in packed bed reactor, Plasma Sources Sci. Technol. 29 (5) (2020), 055004.

[51] K. Van Laer, A. Bogaerts, How bead size and dielectric constant affect the plasma behaviour in a packed bed plasma reactor: a modelling study, Plasma Sources Sci. Technol. 26 (8) (2017), 085007.

[52] M. Salimi, V. Pirouzfar, E. Kianfar, Enhanced gas transport properties in silica nanoparticle filler-polystyrene nanocomposite membranes, Colloid Polym. Sci. 295 (1) (2017) 215–226.

[53] B. Akhavan, M. Croes, S.G. Wise, C. Zhai, J. Hung, C. Stewart, et al., Radical-functionalized plasma polymers: stable biomimetic interfaces for bone implant applications, Appl. Mater. Today 16 (2019) 456–473.

[54] D.A. Hrovat, W.T. Borden, Ab initio calculations of the relative resonance stabilization energies of allyl and benzyl radicals, J. Phys. Chem. 98 (41) (1994) 10460–10464.

[55] F.G. Bordwell, X. Zhang, M.S. Alnajjar, Effects of adjacent acceptors and donors on the stabilities of carbon-centered radicals, J. Am. Chem. Soc. 114 (20) (1992) 7623–7629.

[56] A. Kondyurin, P. Naseri, K. Fisher, D.R. McKenzie, M.M. Bilek, Mechanisms for surface energy changes observed in plasma immersion ion implanted polyethylene: the roles of free radicals and oxygen-containing groups, Polym. Degrad. Stabil. 94 (4) (2009) 638–646.
[57] M. Zhianmanesh, A. Gilmour, M.M.M. Bilek, B. Akhavan, Plasma surface functionalization: a comprehensive review of advances in the quest for bioinstructive materials and interfaces, Appl. Phys. Rev. 10 (2) (2023).
[58] S.G. Wise, H. Liu, A. Kondyurin, M.J. Byrom, P.G. Bannon, G.A. Edwards, et al., Plasma ion activated expanded polytetrafluoroethylene vascular grafts with a covalently immobilized recombinant human tropoelastin coating reducing neointimal hyperplasia, ACS Biomater. Sci. Eng. 2 (8) (2016) 1286–1297.
[59] T.L. Clainche, D. Linklater, S. Wong, P. Le, S. Juodkazis, X.L. Guével, et al., Mechano-bactericidal titanium surfaces for bone tissue engineering, ACS Appl. Mater. Interfaces 12 (43) (2020) 48272–48283.
[60] O.P. Hamill, B. Martinac, Molecular basis of mechanotransduction in living cells, Physiol. Rev. 81 (2) (2001) 685–740.
[61] T. Peng, L. Liu, A.L. MacLean, C.W. Wong, W. Zhao, Q. Nie, A mathematical model of mechanotransduction reveals how mechanical memory regulates mesenchymal stem cell fate decisions, BMC Syst. Biol. 11 (1) (2017) 1–15.
[62] E. Palin, H. Liu, T.J. Webster, Mimicking the nanofeatures of bone increases bone-forming cell adhesion and proliferation, Nanotechnology 16 (9) (2005) 1828.
[63] P.M. Govey, A.E. Loiselle, H.J. Donahue, Biophysical regulation of stem cell differentiation, Curr. Osteoporos. Rep. 11 (2) (2013) 83–91.
[64] V.B. Damodaran, N.S. Murthy, Bio-inspired strategies for designing antifouling biomaterials, Biomater. Res. 20 (1) (2016) 1–11.
[65] A. Sanfeld, C. Royer, A. Steinchen, Thermodynamic, kinetic and conformational analysis of proteins diffusion–sorption on a solid surface, Adv. Colloid Interface Sci. 222 (2015) 639–660.
[66] M.J. Hawker, A. Pegalajar-Jurado, E.R. Fisher, Innovative applications of surface wettability measurements for plasma-modified three-dimensional porous polymeric materials: a review, Plasma Process. Polym. 12 (9) (2015) 846–863.
[67] M. Rodrigues, L.G. Griffith, A. Wells, Growth factor regulation of proliferation and survival of multipotential stromal cells, Stem Cell Res. Ther. 1 (4) (2010) 32.
[68] L. Chen, J. Liu, M. Guan, T. Zhou, X. Duan, Z. Xiang, Growth factor and its polymer scaffold-based delivery system for cartilage tissue engineering, Int. J. Nanomed. 15 (2020) 6097–6111.
[69] Y. Cheng, K.H. Lin, T.H. Young, N.C. Cheng, The influence of fibroblast growth factor 2 on the senescence of human adipose-derived mesenchymal stem cells during long-term culture, Stem Cells Transl Med 9 (4) (2020) 518–530.
[70] S. Tsutsumi, A. Shimazu, K. Miyazaki, H. Pan, C. Koike, E. Yoshida, et al., Retention of multilineage differentiation potential of mesenchymal cells during proliferation in response to FGF, Biochem. Biophys. Res. Commun. 288 (2) (2001) 413–419.
[71] E.R. Edelman, E. Mathiowitz, R. Langer, M. Klagsbrun, Controlled and modulated release of basic fibroblast growth factor, Biomaterials 12 (7) (1991) 619–626.
[72] E.K.A. Nur, I. Ahmed, J. Kamal, A.N. Babu, M. Schindler, S. Meiners, Covalently attached FGF-2 to three-dimensional polyamide nanofibrillar surfaces demonstrates enhanced biological stability and activity, Mol. Cell. Biochem. 309 (1–2) (2008) 157–166.
[73] A. Shakya, E. Imado, P.K. Nguyen, T. Matsuyama, K. Horimoto, I. Hirata, et al., Oriented immobilization of basic fibroblast growth factor: bioengineered surface design for the expansion of human mesenchymal stromal cells, Sci. Rep. 10 (1) (2020) 8762.
[74] D.E. Robinson, L.E. Smith, D.A. Steele, R.D. Short, J.D. Whittle, Development of a surface to enhance the effectiveness of fibroblast growth factor 2 (FGF-2), Biomater. Sci. 2 (6) (2014) 875–882.
[75] J.M. Kang, T. Rajangam, J.W. Rhie, S.H. Kim, Characterization of cell signaling, morphology, and differentiation potential of human mesenchymal stem cells based on cell adhesion mechanism, J. Cell. Physiol. 235 (10) (2020) 6915–6928.
[76] B. Ding, J. Jasensky, Y. Li, Z. Chen, Engineering and characterization of peptides and proteins at surfaces and interfaces: a case study in surface-sensitive vibrational spectroscopy, Acc. Chem. Res. 49 (6) (2016) 1149–1157.
[77] Y.K. Yang, C.R. Ogando, See C. Wang, T.Y. Chang, G.A. Barabino, Changes in phenotype and differentiation potential of human mesenchymal stem cells aging in vitro, Stem Cell Res. Ther. 9 (1) (2018) 131.
[78] S.B. Nandy, S. Mohanty, M. Singh, M. Behari, B. Airan, Fibroblast Growth Factor-2 alone as an efficient inducer for differentiation of human bone marrow mesenchymal stem cells into dopaminergic neurons, J. Biomed. Sci. 21 (1) (2014) 83.
[79] N. Ben Azouna, F. Jenhani, Z. Regaya, L. Berraeis, T. Ben Othman, E. Ducrocq, et al., Phenotypical and functional characteristics of mesenchymal stem cells from bone marrow: comparison of culture using different media supplemented with human platelet lysate or fetal bovine serum, Stem Cell Res. Ther. 3 (1) (2012) 6.
[80] E.M. Horwitz, K. Le Blanc, M. Dominici, I. Mueller, I. Slaper-Cortenbach, F. C. Marini, et al., Clarification of the nomenclature for MSC: the international society for cellular therapy position statement, Cytotherapy 7 (5) (2005) 393–395.
[81] S. Viswanathan, Y. Shi, J. Galipeau, M. Krampera, K. Leblanc, I. Martin, et al., Mesenchymal stem versus stromal cells: international society for cell & gene therapy (ISCT(R)) mesenchymal stromal cell committee position statement on nomenclature, Cytotherapy 21 (10) (2019) 1019–1024.
[82] S.-M. Han, S.-H. Han, Y.-R. Coh, G. Jang, Ra J. Chan, S.-K. Kang, et al., Enhanced proliferation and differentiation of Oct4-and Sox2-overexpressing human adipose tissue mesenchymal stem cells, Exp. Mol. Med. 46 (6) (2014) e101–e.
[83] I. Jyothilekshmi, N.S. Jayaprakash, Trends in monoclonal antibody production using various bioreactor syst, J. Microbiol. Biotechnol. 31 (3) (2021) 349–357.
[84] J. Gobin, G. Muradia, J. Mehic, C. Westwood, L. Couvrette, A. Stalker, et al., Hollow-fiber bioreactor production of extracellular vesicles from human bone marrow mesenchymal stromal cells yields nanovesicles that mirrors the immuno-modulatory antigenic signature of the producer cell, Stem Cell Res. Ther. 12 (1) (2021) 127.
[85] S.B. Cheng, M. Wang, C. Zhang, M.M. Chen, Y.K. Wang, S. Tian, et al., Flexible three-dimensional net for intravascular fishing of circulating tumor cells, Anal. Chem. 92 (7) (2020) 5447–5455.